Numerical simulation of InN based HEMTs

Master's thesis in Erasmus Mundus Master of Nanoscience and Nanotechnology
Option nanoelectronics

MICHIEL VANDEMAELE

Examiners / promoters:
Assoc. prof. Niklas Rorsman, Chalmers University of Technology
Prof. dr. ir. Dominique Schreurs, KU Leuven

Department of Microtechnology and Nanoscience
CHALMERS UNIVERSITY OF TECHNOLOGY
Gothenburg, Sweden 2015

Master's thesis 2015

Numerical simulation of InN based HEMTs

MICHIEL VANDEMAELE

Department of Microtechnology and Nanoscience
Microwave Electronics Laboratory
Chalmers University of Technology
Gothenburg, Sweden 2015

Numerical simulation of InN based HEMTs
MICHIEL VANDEMAELE

© MICHIEL VANDEMAELE, 2015.

This thesis was carried out as part of the Erasmus Mundus Master of Nanoscience and Nanotechnology, option nanoelectronics. The author of this thesis followed the first year of the master at KU Leuven and the second year at Chalmers University of Technology.

Supervisor:
Assoc. prof. Hans Hjelmgren, Department of Microtechnology and Nanoscience, Chalmers University of Technology

Examiner (promoter):
Assoc. prof. Niklas Rorsman, Department of Microtechnology and Nanoscience, Chalmers University of Technology

Co-promoter:
Prof. dr. ir. Dominique Schreurs, Department of Electrical Engineering,
KU Leuven

Master's Thesis 2015
Department of Microtechnology and Nanoscience
Microwave Electronics Laboratory
Chalmers University of Technology
SE-412 96 Gothenburg
Telephone +46 31 772 1000

Typeset in LaTeX
Gothenburg, Sweden 2015

Numerical simulation of InN based HEMTs
MICHIEL VANDEMAELE
Department of Microtechnology and Nanoscience
Chalmers University of Technology

Abstract

Invented in 1980, High Electron Mobility Transistors (HEMTs) are now widely used in high-frequency electronics. They are fabricated in different material systems and a possible new material for future devices is indium nitride (InN). InN HEMTs are considered very promising because of the good electron transport properties of the material predicted by Monte Carlo simulations. InN has a lower effective mass, higher mobility and higher peak drift velocity than GaN. Compared to (In)GaAs, the material also performs well. However, due to current problems with the InN material growth, the field of InN HEMTs is still at an early stage.

This master's thesis reports (one of) the first numerical simulations of InN HEMTs. It covers the implementation of a simulation model for such a device starting from a theoretical proposal in the literature. Its DC and AC output are analysed and compared to analytical calculations. Based on the agreement between both, it is concluded that the simulation model works correctly. The model was used to extract the potential performance of an InN HEMT. Using the best parameters and for a gate length of 100 nm, an extremely high f_t and $f_{\max}$ of 400 and 430 GHz are obtained, respectively. However, it is also noted that these values depend a lot on the assumed high saturation velocity used in the model. At the end of the project, the simulation deck was also used to simulate some other InN HEMT structures.

Keywords: indium nitride (InN), III-nitrides, HEMT, numerical simulations, TCAD.

Acknowledgements

Writing a master's thesis is not an easy task. During the process, many questions and problems pop up. Having different people around you to whom you can ask questions and who guide you is therefore a big help. Without these people, this master's thesis would not have been possible. At the end of the project, it is a pleasure to say thank you to all of them.

First of all, I would like to express my gratitude to assoc. prof. Niklas Rorsman for being my examiner and offering me this very broad and interesting master's thesis project. Thanks to my supervisor assoc. prof. Hans Hjelmgren for guiding me through the project and helping me working it out starting from some basic ideas to this final report. I am also grateful to prof. dr. ir. Dominique Schreurs for agreeing to be my KU Leuven co-promoter and following the work from Belgium.

Next, I would like to thank everybody at the Microwave Electronics Laboratory for creating a stimulating and pleasant work environment. Special thanks to Henric for setting up the simulation software on my computer and to Olle and Dhecha for taking me to lunch and afterwork. I would like to thank assis. prof. Mattias Thorsell for giving feedback on my presentation. Thanks also to assoc. prof. Tommy Ive of the Photonics Laboratory for explaining me the challenges of InN growth and answering my questions related to this.

The experimental data of the InN samples grown at Chalmers University of Technology reported in this master's thesis are the work of assoc. prof. Niklas Rorsman and assoc. prof. Tommy Ive and I would like to acknowledge this support.

Furthermore, I would like to say thank you to the responsibles of the EMM nano programme and the universities Chalmers and KU Leuven for giving me the opportunity to follow this master's programme and study the last year of my master abroad. This year in Sweden was a very enriching period for me personally. Thanks also to my friends here in Sweden and Belgium for the fine study time we had together.

Finally, I would like to thank my family for their continuous support, both in times when things were going well and less well.

Thank you!
Tack så mycket!
Dankjewel!

Michiel Vandemaele, Gothenburg, June 2015

Contents

Abstract i

Acknowledgements iii

List of Figures vii

List of Tables ix

1 Introduction 1
- 1.1 InN as material for high-frequency electronics . . . 1
- 1.2 Objective of the master's thesis and structure of the report . . . 2

2 Theoretical background 5
- 2.1 Material properties of InN . . . 5
- 2.2 Growth of InN . . . 9
- 2.3 Origin of the unintentional doping . . . 9
- 2.4 HEMTs . . . 12
- 2.5 Transport models . . . 15

3 Basic simulation model 17
- 3.1 Structure of the InN HEMT . . . 17
- 3.2 Basic physical effects included . . . 18
- 3.3 Output and verification of the basic model . . . 22
- 3.4 Performance extraction and remarks . . . 26

4 Extended simulation model 31
- 4.1 Electrons, holes and quantization effects . . . 31
  - 4.1.1 Origin of electrons . . . 31
  - 4.1.2 Quantization effects . . . 33
- 4.2 Detailed mobility model . . . 35
  - 4.2.1 Unintentional doping dependent mobility . . . 35
  - 4.2.2 Saturation velocity . . . 38
  - 4.2.3 Updated performance extraction . . . 40
- 4.3 Other InN HEMT structures . . . 41
  - 4.3.1 InN/GaN structure . . . 41
  - 4.3.2 AlN/InN/GaN structure . . . 45

5 Conclusions **49**
5.1 The simulation model 49
5.2 Performance and other designs of InN HEMTs 50
5.3 Future outlook 51

Bibliography **53**

A Device definition normally-off InN HEMT **I**

B Device simulation normally-off InN HEMT **V**

C Material parameters normally-off InN HEMT **IX**

List of Figures

2.1 Optical bandgap $E_G + E_F$ versus electron concentration of InN samples. 6
2.2 Schematic picture of the wurtzite crystal structure of InN and graph of bandgap versus lattice constant for the III-nitrides. 7
2.3 Steady-state and transient electron transport characteristics of bulk InN. 8
2.4 Hall mobility and carrier concentration at room temperature for MOVPE and MBE grown InN epilayers. 10
2.5 Energy levels and electron occupancies of neutral defects in InN and their formation energy versus the Fermi level position. 11
2.6 Relation between electron concentration and threading dislocation density in InN. 12
2.7 Schematic cross-section of a HEMT. 13
2.8 Illustration of the formation of a heterojunction between two different semiconductor materials. 14

3.1 Cross-section of the normally-off InN HEMT as implemented in the basic simulation model. 18
3.2 Comparison of the different electron $v(E)$ models used in this and other works. 22
3.3 Band diagram and electron concentration profile of the normally-off and normally-on HEMT. 23
3.4 $I_d(V_d)$ characteristic of the normally-off HEMT. 24
3.5 $I_d(V_d)$ characteristic of the normally-on HEMT. 25
3.6 $I_d(V_g)$ curves for the normally-off and normally-on HEMT. 26
3.7 Smith chart/polar plot of the S-parameters of the normally-on HEMT in the basic model. 27
3.8 Amplitude of the S-parameters S_{12} and S_{21} in dB of the normally-on HEMT in the basic model. 27

4.1 Illustration of the 2DHG at the bottom of the InAlN buffer responsible for the electrons in the InN channel. 32
4.2 Influence of the variation of γ_{e^-}(InN) and γ_{e^-}(GaN) on the electron concentration profile in the channel and GaN spacer. 34
4.3 Error of the fit of the electron concentration profile versus γ_{e^-}(InN) and γ_{e^-}(GaN). 34
4.4 Band diagram and electron concentration profile in the channel after the addition of the density gradient method to the model. 35

4.5 Mobility μ versus unintentional doping level/ionized impurity concentration N_d in bulk InN. 37
4.6 $I_d(V_d)$ curve of the normally-on HEMT in the basic model with v_{sat} equal to the real saturation velocity of 1.6×10^7 cm/s. 39
4.7 $I_d(V_g)$ curve of the normally-on HEMT in the basic model with v_{sat} equal to the real saturation velocity of 1.6×10^7 cm/s. 39
4.8 Performance of the InN HEMT for different levels of the unintentional doping. 41
4.9 Structure and band diagram of the first InN samples grown at Chalmers University of Technology. 42
4.10 Measured and calculated sheet charge density n_s of InN samples versus thickness t of the InN layer. 43
4.11 Band diagram of the first InN samples grown at Chalmers University of Technology, but with N-polarity for all the III-nitrides. 45
4.12 Structure and band diagram of the AlN/InN/GaN stack. 46
4.13 $I_d(V_g)$ curves for the AlN/InN/GaN structure and threshold voltage V_T and voltage $V_{g_m=0}$ at which the slope of the $I_d(V_g)$ curve becomes zero versus thickness t' of the AlN layer. 47
4.14 $I_d(V_g)$ curve of the Kuzmík InN HEMT proposal for different channel thicknesses t and $I_{\mathrm{on}}/I_{\mathrm{off}}$ ratio in function of channel thickness for different gate lengths. 48

List of Tables

1.1 Overview of the electron transport parameters of different materials used in (high-frequency) electronics. 2

2.1 Comparison of InN transport parameters calculated by different Monte Carlo simulations using the new bandgap and effective mass value. . . 8
2.2 Overview of f_t and $f_{\max}$ of different experimental HEMTs. 15

3.1 Horizontal and vertical dimensions of the normally-off HEMT. 19
3.2 Overview of different material parameters used in the basic simulation model. 19
3.3 Overview of the InN transport parameters used in the basic simulation model. 19
3.4 Comparison of the values for the surface polarization charges in the normally-off HEMT in [10] and in this work. 23
3.5 Overview of the threshold voltage V_T and transconductance g_m of the normally-off and normally-on HEMT in [10] and this work. 25
3.6 Overview of f_t and f_{max} of the normally-on HEMT in the basic model and the bias point at which the values are obtained. 28

4.1 Overview of the values for the different parameters in the empirical model describing the low-field mobility in function of the unintentional doping level for bulk InN. 37
4.2 Performance of the InN HEMT for an unintentional doping level of 10^{14} cm^{-3}. 41
4.3 Material parameters for Al_2O_3. 42
4.4 Overview of the magnitude of the polarization vector $\vec{P}$ in the III-nitride layers and the interface charges σ at the interfaces between these layers for the structures grown at Chalmers University of Technology. 44
4.5 Overview of the magnitude of the polarization vector $\vec{P}$ in the III-nitride layers and the interface charges σ at the interfaces between these layers for the AlN/InN/GaN structure. 47

1

Introduction

Invented in 1980 [1], a High Electron Mobility Transistor (HEMT), also called Heterostructure Field Effect Transistor (HFET) or MOdulation-Doped FET (MODFET), is a type of transistor using a heterostructure of two semiconductor materials with different bandgap to physically separate the electrons in the channel from the donors in the barrier. In this way, it avoids degradation of the mobility by impurity scattering. Combining materials inherently having a high mobility with this 'trick' makes HEMTs very fast. As a consequence, they find application in high-frequency circuits.

This master's thesis reports numerical simulations of HEMTs based on indium nitride (InN), a very promising material for future high-frequency electronics. The first section of this chapter discusses the (possible) position of InN among the different materials currently used for high-frequency circuits. Then, the second section explains the actual objective of the thesis and summarizes the structure of this report.

1.1 InN as material for high-frequency electronics

At this moment, the semiconductor InN is not used in high-frequency electronics. However, InN has an extreme potential to do so in the future. Different Monte Carlo simulations [2–5] predict very attractive electron transport properties for this material. As table 1.1 shows, InN has a low effective mass, high mobility and high peak drift velocity compared to GaAs, InGaAs and GaN, the three main materials used as channel of commercial HEMTs today. One can imagine different functions for InN in high-frequency electronics and the next paragraphs discuss them.

From a technology point of view, it is quite natural to envision a role for InN as a possible improvement for GaN HEMTs. The reason is that InN belongs to the III-nitrides, the material family used in GaN technology. Since its introduction on the market in 2005 [6], the original AlGaN/GaN heterostructure has been changed several times to increase performance. Changes included the insertion of an AlN spacer between the AlGaN barrier and GaN channel to enhance the mobility [7] and the replacement of AlGaN with InAlN to increase the sheet electron density n_s [8]. Given the good transport properties of InN, one possible route towards further performance improvement could be replacement of the GaN in the channel with InN.

Unlike GaN, InN has a relatively small bandgap, as illustrated by table 1.1. The high bandgap of GaN makes the material perfect for high-power (high-speed)

Table 1.1: Overview of the electron transport parameters of different materials used in (high-frequency) electronics. For the InN mobility, (T) and (M) mean theoretical and measured value, respectively. Data for InGaAs are for $In_{0.53}Ga_{0.47}As$. Effective mass for Si is an average of the longitudinal and transverse effective mass. (data from [2, 12–17])

	Si	GaAs	InGaAs	GaN	InN
E_g (eV)	1.12	1.42	0.81	3.43	0.7
$m_{\text{eff},n}$ (m_0)	0.328	0.067	0.041	0.2	0.042
μ_n (cm^2 V^{-1} s^{-1})	1400	8500	12000	1000 - 2000	2000 (M) - 10 000 (T)
$v_{\text{peak},n}$ (10^7 cm/s)	1	2	2.8	2.9	6.0
$v_{\text{sat},n}$ (10^7 cm/s)	1	0.72	0.6	1.9	1.4

circuits [9]. Therefore, from an application point of view, InN possibly has to be viewed less as a competitor for GaN HEMTs and more for the high speed GaAs- and InP-based HEMTs [7]. Different observations motivate the idea that InN HEMTs should have speed performance similar to GaAs- and InP-based devices. As shown in table 1.1, InN has comparable steady-state transport properties as GaAs and InGaAs. Besides, studies also predict very good transient electron transport for InN. According to [2], InN has higher velocity overshoot than GaAs (and GaN).

The above considerations illustrate that InN is a very promising material. Despite its remarkable potential, research on InN HEMTs is still at an early stage. There are some theoretical proposals for InN HEMTs in the literature (e.g. [10, 11]), but (almost) no practical realisations of such devices. The major reason for this is the growth of the material which is still immature. State-of-the-art InN layers suffer from high unintentional *n*-doping and corresponding low mobility, as indicated by the difference between theoretical and measured mobility in table 1.1 [12].

1.2 Objective of the master's thesis and structure of the report

The objective of this master's thesis is to investigate InN HEMTs using numerical simulations. A commercial simulator for semiconductor devices, Sentaurus TCAD from Synopsys (version J-2014.09), will be used. Very specifically, the master's thesis addresses the following research question:

> Which parameters are needed to build a computer model for an InN HEMT, which physical effects should this computer model include and what performance does it predict?

Analysing the research question reveals the two tasks to be carried out in this master's thesis project. First of all, building a computer model for a InN HEMT is an important part of the work. This includes the selection of the necessary parameters and physical effects to describe the device. The second task consists of using this model to extract the (potential) performance of an InN HEMT.

The following considerations motivate the objective of this thesis. As mentioned above, not so much research on InN HEMTs has been done up to now. There are some theoretical proposals for InN HEMT structures in the literature, but sometimes they do not contain estimates for the current [11] or f_t, $f_{\mathrm{max}}\ldots$ [10, 11]. Computer simulations are a useful tool to estimate these figures of merit. In this way, an overview on the potential performance of InN HEMTs can be obtained, which may be helpful when assessing if investing time and resources in InN growth improvement is worth the effort.

Besides that, building the computer model itself is a useful result. Once the material growth has improved in such a way that practical devices become feasible, the model can be used to support the design of InN HEMTs. It can help interpreting experimental results and optimizing the structure. Furthermore, it can give insight in the physics and operation of this new device.

This report describes the results of the master's thesis project. It is organized as follows. Chapter 2 gives some theoretical background on the material InN and on HEMTs. Next, chapter 3 discusses the implementation of a basic simulation model for an InN HEMT, starting from a theoretical proposal in the literature. In chapter 4, the basic model is refined and subjected to further investigation. These two chapters also describe the potential performance of InN HEMTs using the basic and extended simulation model. Finally, chapter 5 concludes the thesis by summarizing the obtained results.

2

Theoretical background

This chapter gives some theoretical background on the topic of the master's thesis. The first section summarizes important material properties of InN, mainly structural and electrical ones. The next two sections consider at length the growth of InN and the origins of the high unintentional doping in the material. Then, the text discusses the operation principle and figures of merit of HEMTs. The last section closes the chapter by providing an overview of the simulation models used in this master's thesis.

2.1 Material properties of InN

Many properties of InN are already summarized in table 1.1 and this section discusses them in detail. First of all, the most important parameter of any semiconductor is its bandgap. InN is a direct gap semiconductor with a rather small bandgap of around 0.7 eV, as pointed out in 2002 by Davydov et al. [18]. They combined absorption, photoluminescence and photoluminescence excitation spectra of different single-crystalline wurtzite InN layers to draw their conclusion. This discovery was quite surprising, since before all measurements had indicated a larger bandgap of (around) 1.89 eV. Other groups confirmed the results of Davydov et al. around the same time [19].

Different explanations are given in the literature for the observance of the larger bandgap in the past and the smaller one now, all with pros and cons. The following paragraphs briefly list the ones given by Davydov et al. They mentioned the influence of the presence of oxynitrides in the samples with larger bandgap as main reason [18]. They analysed different samples with a claimed bandgap around 1.89 eV and found that these had poorer (structural) quality and oxygen contents up to 20%, compared to 1% in their own small bandgap samples. Since oxynitrides have a bandgap of around 2 eV at approximate oxygen concentrations in the sample of 20%, they concluded that the oxynitrides may be responsible for the observation of the larger bandgap. In [20], it was indicated that oxynitrides can indeed have an influence, but it was emphasized that further investigation is needed to draw this conclusion.

Another explanation quoted for the difference is the Burstein-Moss effect. This phenomenon occurs in degenerate semiconductors and is important when measuring the bandgap through optical absorption experiments [18], i.e. when measuring the so called optical bandgap. If the Fermi level lies in the conduction band, incident photons need an energy larger than the true band gap energy to excite electrons

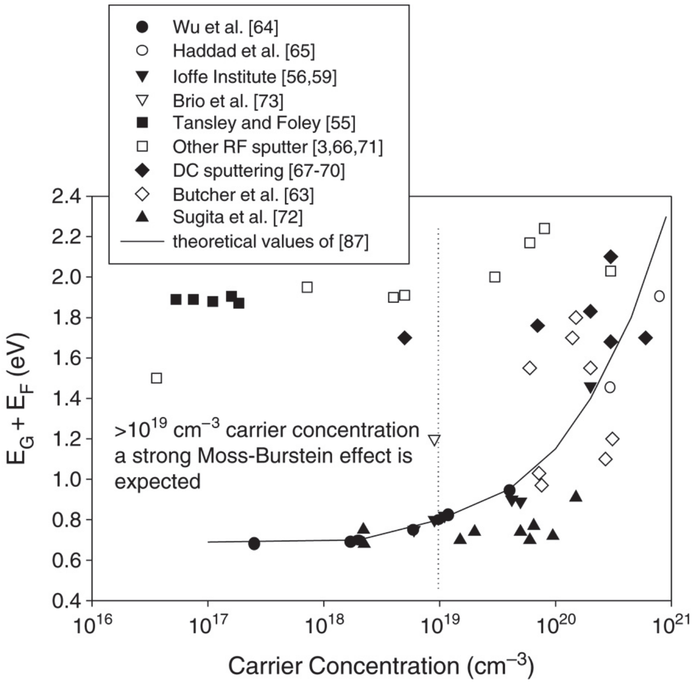

Figure 2.1: Optical bandgap $E_G + E_F$ (i.e. bandgap as measured by optical absorption measurements) versus electron concentration of InN samples. The full curve is the optical bandgap that is expected when taking the Moss-Burstein effect into account. (from [20]. Reference numbers in the fig. are from the references in [20].)

from valence to conduction band. Indeed, the conduction band minimum is now occupied with electrons and photons will only be absorbed if their energy is sufficient to bring an electron from the valence band maximum to the Fermi level located above the conduction band minimum. This causes an increase in the energy onset at which optical absorption occurs, i.e. in the absorption edge or optical bandgap, with increasing electron concentration. As a consequence, the real bandgap is overestimated by the absorption measurement [21].

The Burstein-Moss effect is a plausible explanation for the observed difference in bandgap, since InN layers suffer from high background electron concentration, as explained in the next sections, and since the larger bandgap values had been determined exclusively by optical absorption measurements [19]. Fig. 2.1 confirms this by plotting the measured optical bandgap of samples with different electron concentration together with the expected value assuming a 0.7 eV bandgap and the presence of the Moss-Burstein effect. According to [21], the effect can explain the difference completely, whereas [20] emphasizes that it is only a partial explanation.

Related to the bandgap/bandstructure is the electron effective mass, another important semiconductor parameter. However, due to the InN bandgap revision, there is uncertainty about its exact value [5]. Based on a theoretical reasoning using the new bandgap, a value of 0.042 m_0 is found [17]. The argument is that for direct gap semiconductors the electron effective mass varies approximately linearly with the bandgap. In order for InN to follow this trend, 0.042 m_0 should be the mass. This is the lower limit cited in the literature with other values ranging over 0.07 m_0 also taking the new bandgap into account [21] up to 0.11 m_0 measured before the

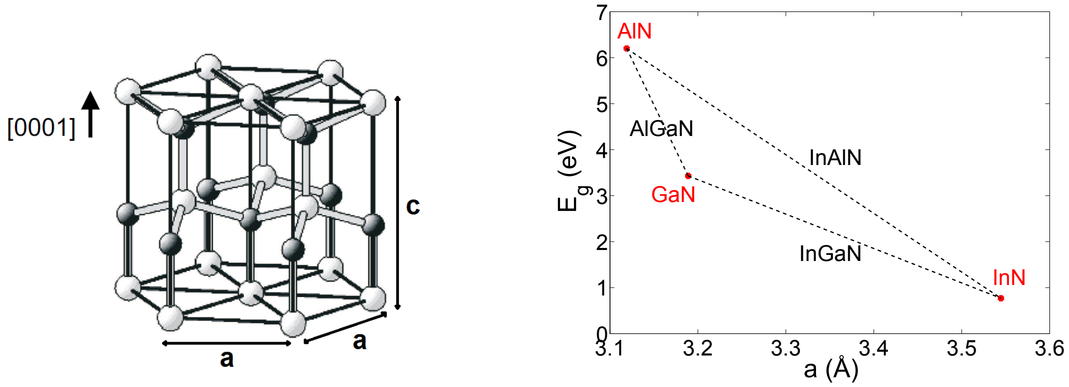

Figure 2.2: Schematic picture of the wurtzite crystal structure of InN (left). White atoms are In, black ones are N. Remark that in reality the In atoms are larger than the N ones. Bandgap E_g versus lattice constant a for the III-nitrides (right). (left fig. from [24], slightly adapted; data for right fig. from [16])

bandgap revision [22]. Bandgap (and effective mass) further have an influence on the calculation of the nonparabolicity coefficient α of the lowest conduction band valley [5, 21]. As a consequence, there also exist uncertainty about the value for α.

With respect to structural parameters, the crystal structure is important to know. At room temperature, InN has, just as the other nitrides GaN and AlN, a wurtzite crystal. It is characterised by a lattice constant $a_0 = 3.54$ Å along the a-axis and $c_0 = 5.705$ Å along the c-axis [16]. The left panel of fig. 2.2 is a schematic picture of the wurtzite crystal structure and the right panel compares the lattice constant and bandgap of the III-nitrides. Notably, the InN lattice constant is substantially larger than the GaN and AlN one. Mostly, III-N semiconductors are grown with the c-axis perpendicular to the substrate, resulting in either In/Ga/Al-face material in case In/Ga/Al-atoms form the top layer or N-face in case N-atoms do this [23]. The former is also called cation-face and the latter anion-face.

Characteristic for III-nitrides, including InN, are their very large (much larger than for other semiconductors) electrical polarization effects. In the absence of an external electric field, the macroscopic polarization $\vec{P}$ of a III-N layer consists of a spontaneous $\vec{P}_{\mathrm{SP}}$ and piezoelectric part $\vec{P}_{\mathrm{PE}}$. The spontaneous part is always present and originates from the polar bonds and the specific crystal structure of III-nitrides. It is oriented along the c-axis, with different direction (up/down) for cation- and anion-face layers. The piezoelectric part originates from the direct piezoelectric effect and is only present when the layer is strained on an underlying layer. The magnitude of the piezoelectric polarization along the c-axis is given by:

$$P_{\mathrm{PE}} = 2\left(\frac{a - a_0}{a_0}\right)\left(e_{31} - e_{33}\frac{C_{13}}{C_{33}}\right) \tag{2.1}$$

Here, a and a_0 are the strained and equilibrium lattice constant, e_{13} and e_{33} are piezoelectric coefficients and C_{13} and C_{33} are elastic constants respectively [23, 24].

Finally, the InN transport parameters (low-field mobility, saturation and peak drift velocity) are discussed. Values for them can be obtained from Monte Carlo

Table 2.1: Comparison of InN transport parameters calculated by different Monte Carlo simulations using the new bandgap and effective mass value. For comparison, a variational principle calculation using the old value for the bandgap and effective mass is given (study 5). All values are given for 300 K. μ_{max} is the theoretically maximum mobility.

		1 [2]	2 [4]	3 [5]	4 [3]	5 [25]
Input	E_g (eV)	0.75	0.7	0.8	0.7	1.9
	m_{eff} (m$_0$)	0.045	0.04	0.042, 0.07	0.04	0.115
	α (eV^{-1})	0.4, 1.22	1.43	1.147, 1.081	1.43	/
	N_d (cm^{-3})	10^{17}	10^{16}	10^{17}	10^{17}	/
Output	μ (cm^2 V^{-1} s^{-1})	/	7500	8800, 5800	4800	/
	μ_{max} (cm^2 V^{-1} s^{-1})	10000	/	10000, 6700	14000	4400
	v_{peak} (10^7 cm/s)	6.0, 5.9	6.1	5.1, 4	5.3	/
	v_{sat} (10^7 cm/s)	1.4, 1.75	1.9	1.5	1.3	/

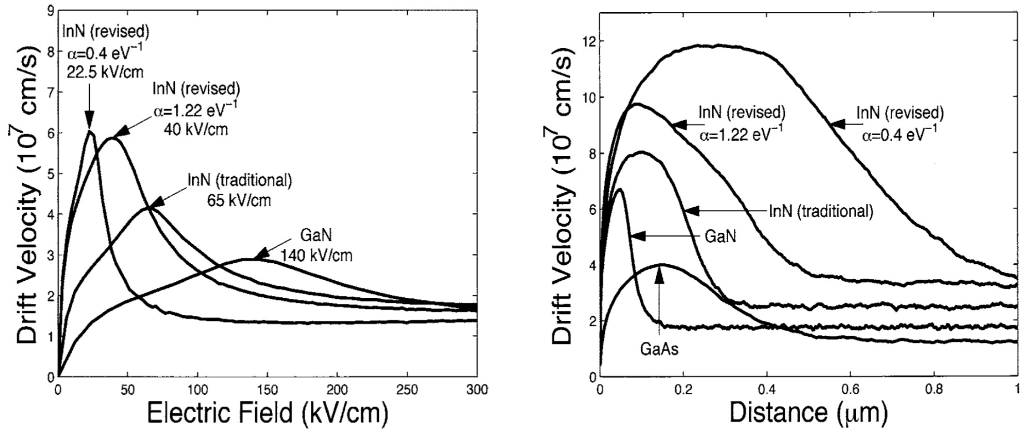

Figure 2.3: Steady-state (left) and transient (right) electron transport characteristics of bulk InN. α is the nonparabolicity coefficient of the lowest-energy conduction band valley. The curves in the right panel are for different electric fields (two times the electric field mentioned in the left panel). (from [2])

simulations. Bandgap, effective mass and the nonparabolicity coefficient α are important input parameters for such simulations. As a result, calculations using the old band structure parameters give significantly different results than the ones using the new values. Based on the old parameters, InN had already good transport characteristics and with the new parameters Monte Carlo simulations indicate even better results [2, 5].

Table 2.1 lists different Monte Carlo results for steady-state electron transport in InN and is a refinement of table 1.1. Scattering mechanisms taken into account in all four studies are intervalley, ionized impurity and acoustic and optical phonon scattering [5]. Fig. 2.3 shows the steady-state velocity-field and transient velocity characteristics. The latter indicates that InN has considerably higher velocity overshoot than GaN and GaAs. However, an important remark is that all the Monte Carlo results still need experimental verification. As an example, the high mobilities have not been observed (yet) due to problems with the InN growth. Although different groups predict the high values, only experimental observation can ultimately confirm their correctness.

2.2 Growth of InN

As mentioned in chapter 1, problems with the growth of InN currently prevent its use in high-frequency electronics. InN has a very low dissociation temperature ($\leq$ 600 °C [16]). To grow the material it is of course necessary to stay below this dissociation temperature and the requirement of low growth temperature makes InN growth very difficult.

There are two main growth techniques for InN: MetalOrganic Vapour Phase Epitaxy (MOVPE) and Molecular Beam Epitaxy (MBE). MOVPE mostly uses trimethylindium (TMI) as In-source, ammonia (NH_3) as N-source and nitrogen gas (N_2) as carrier gas. It suffers from a low growth rate, caused by the low dissociation rate of NH_3 at the low InN growth temperature (500 - 650 °C) [19].

MBE mostly uses solid sources of In and gas sources of N (N_2 or NH_3) [19]. A plasma is used to generate atomic reactive N. In this way, the formation of N radicals becomes independent of the InN growth temperature, which is an advantage compared to MOVPE [16]. The growth temperature can be chosen lower than necessary to dissociate N_2 or NH_3 and is usually 450 - 550 °C [19].

There is no lattice matched substrate for InN. To solve this, a buffer layer grown at low temperature is inserted between the substrate and the InN epilayer, similar as for GaN growth. The most common substrate is sapphire [12, 19].

Grown InN layers suffer from high background electron concentrations, ranging from 10^{17} to 10^{20} electrons per cm^3, as shown in fig. 2.4. This high unintentional doping degrades the electron transport properties of the material. As fig. 2.4 shows, it is also correlated with the thickness of the InN layers. In general, epilayers grown by MBE show better quality than the ones grown by MOVPE. The lowest background electron concentration ever achieved for the former is 3.5×10^{17} cm^{-3} with a mobility of 2050 cm^2 V^{-1} s^{-1}, compared to 4×10^{18} cm^{-3} and 1180 cm^2 V^{-1} s^{-1} for the latter [12]. Besides high bulk electron concentration, experiments indicate the presence of an electron accumulation layer on the InN surface [26].

2.3 Origin of the unintentional doping

As mentioned in the previous section, all grown InN layers to date are unintentionally n-doped. The exact origin of the high n-doping is not known. Several possibilities exist, but there is no consensus about which one is responsible [19, 26, 27].

A first possibility is that native point defects in the InN lattice donate electrons to the conduction band. Theoretical calculations by Jenkins and Dow [28], using the old bandgap value, showed that N-vacancies (missing N-atoms) act as donors in InN. As shown in the left panel of fig. 2.2, every N-atom in the wurtzite structure is surrounded by four In-atoms. A missing N-atom thus means that three In-atoms each have one surplus valence electron. According to the calculations of Jenkins and Dow, shown in the left panel of fig. 2.5, one (and possibly all three) of these electrons occupy states in the conduction band, making the N-vacancy a single (or possibly triple) donor. Jenkins and Dow also investigated In-vacancies and antisites (a N-atom on an In-site or vice versa), but found that none of them acts as donor

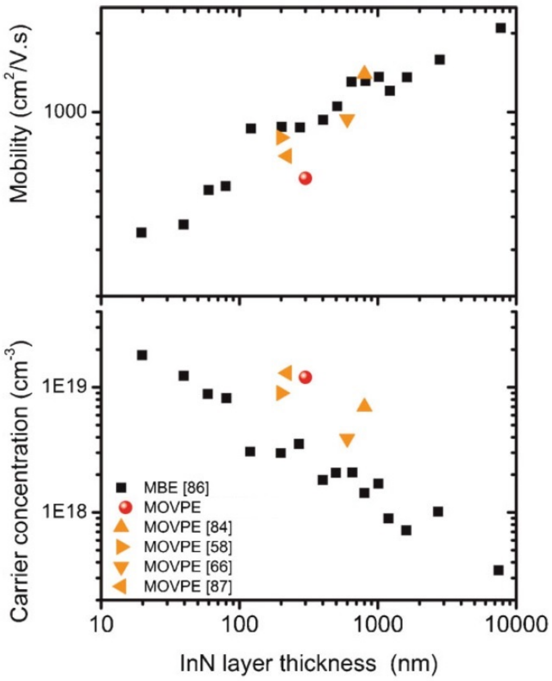

Figure 2.4: Hall mobility and carrier concentration at room temperature for MOVPE and MBE grown InN epilayers. (from [12], slightly adapted. Reference numbers in the fig. are from the references in [12].)

in InN. As the left panel of fig. 2.5 illustrates, the energy levels of In-vacancies lie close to the valence band, making it a triple acceptor, and the ones of both N- and In-antisites lie more in the middle of the gap, making them deep traps for electrons and holes. The important conclusion was that N-vacancies can be responsible for the high *n*-doping [19, 28]. Intuitively, this sounds plausible since supply of reactive N is a problem in (MOVPE) growth of InN. In general, the carrier concentration decreases with higher NH_3/TMI ratio in MOVPE growth [19].

Van de Walle et al. [26] did first principles calculations more recently, taking the new bandgap into account. They calculated the formation energy of the different types of defects and the right panel of fig. 2.5 shows their results. They confirmed that a N-vacancy can be a single or triple donor. However, they concluded that the formation energy of this defect is too high to have a concentration of them large enough to explain to observed electron concentrations. Since InN is *n*-type, the Fermi-level must lie close to the conduction band minimum. As the right panel of fig. 2.5 shows, this corresponds to a formation energy of 1 eV, resulting in a concentration of N-vacancies of 4×10^{15} cm^{-3}, which is much lower than the lowest observed electron concentration in InN. They also investigated other defects, but found that these all have higher formation energies and hence lower concentrations than the N-vacancy. Therefore, Van de Walle et al. concluded that native point defects are probably not the reason for the high n-type doping [26].

A second possibility is unintentional doping by impurities, such as oxygen, silicon and hydrogen [19]. Oxygen atoms on a N-site and silicon atoms on an In-site both have one excess electron that they can donate to the conduction band. Theoretical calculations [26] revealed that incorporation of oxygen or silicon atoms in

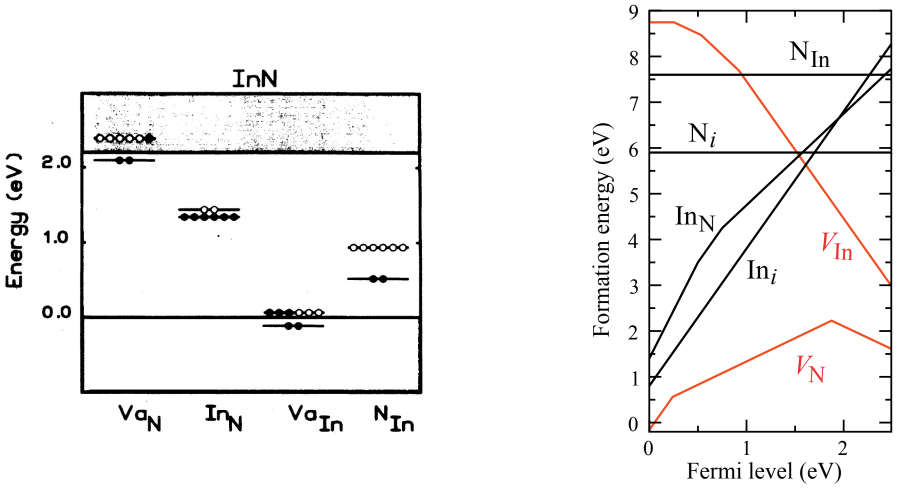

Figure 2.5: Band diagram of InN (with the old value for the bandgap) indicating the energy levels and electron occupancies of neutral defects in the material (left). Formation energy of defects in InN versus the Fermi level position (right). A Fermi level equal to zero is located on the valence band maximum. (left fig. from [28], slightly adapted; right fig. from [26])

the InN lattice has a much lower formation energy than nitrogen vacancies, meaning that the impurities should be present in higher concentrations than the vacancies. These observations, together with the fact that oxygen is often present in growth environments and that oxygen and silicon are donors in GaN, make these impurities a plausible explanation for the high n-doping in InN [26].

Another impurity considered as being responsible is hydrogen. First principles studies [26] indicate that H can occupy interstitial and N-positions in the InN lattice, in which case it is a single or double donor respectively. The behaviour of interstitial H in InN is different from the one in most semiconductors, where it is an amphoteric defect (it can be both donor and acceptor). The calculations again indicate that the formation energy for H incorporation is lower than for N-vacancies when the Fermi level is at the conduction band minimum, meaning that the former should be present in much higher concentration. Considering that H is present in many growth environments (even in ultrahigh vacuum MBE systems), it is another good candidate to explain the n-doping in InN [26, 27].

Besides theoretical studies, there exist also experimental investigations of impurities in InN. In [27] e.g., secondary ion mass spectrometry (SIMS) measurements were performed on plasma assisted MBE grown InN samples. The important observation in this work was that the oxygen and hydrogen concentration was comparable (in case of In-rich growth) or higher (in the case of N-rich growth) than the electron concentration, meaning that they can explain the n-doping. However, in the case of N-rich growth, no explanation was given why not all impurities would be active as donor.

Next, also threading dislocations are sometimes cited as a possible explanation. In [29], different InN samples were grown by plasma-assisted MBE. Using full width at half maximum (FWHM) values of measured X-ray rocking curves (XRC), edge-component threading dislocation densities in the samples and densities of dangling bonds along these dislocations were calculated. For electron concentrations up to

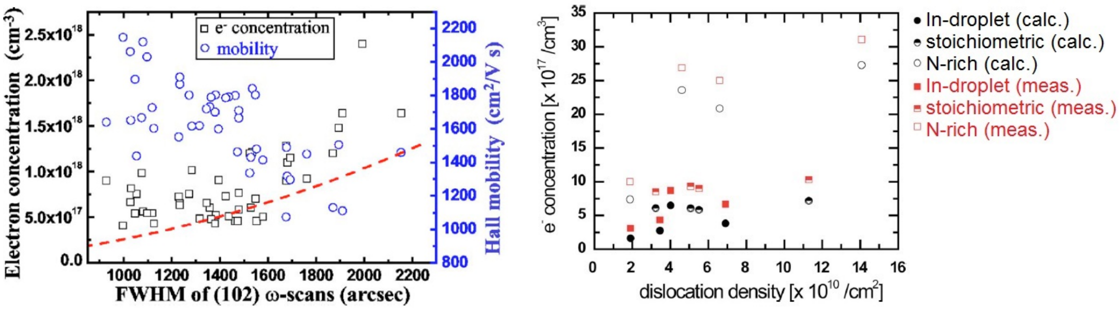

Figure 2.6: Relation between electron concentration and threading dislocation density in InN according to two different studies. In the left fig., the dashed line shows the estimated density of dangling bonds along the dislocations and should be read on the left axis. In the right fig., the difference between calculated and measured values is that the former does not included the effect of the InN electron surface accumulation layer. This is also the case for all the values in the left fig. (left fig. from [29]; right fig. from [27], slightly adapted)

2.5×10^{18} cm^{-3}, agreement between the density of dangling bonds along dislocations and bulk electron concentration was observed, leading to the conclusion that the former may be the origin of the latter.

Something similar was done in [27], using almost the same experimental techniques, but leading to the opposite conclusion, because no dependence of electron concentration on dislocation density was observed. Fig. 2.6 shows the results of both studies ([29] left, [27] right). Although the density of dangling bonds along the dislocations qualitatively follows the trend of the electron concentration in [29], it often underestimates the carrier density by a factor 2.5 (sometimes 4). The authors speculated that also taking the contributions from impurities and native defects into account could close the gap. Also note that both studies consider only a limited range of electron concentrations. Despite the disagreement on the role on electron concentration, both studies found that the dislocations do have an influence on electron mobility.

Having discussed the different possibilities for the *n*-doping, it is possible to explain why MBE grown films in general have better properties than MOVPE ones. An intuitive explanation is that MBE is characterized by reduced impurity incorporation (due to a.o. the use of ultra-high vacuum) and N-supply independent of growth temperature, leading to less lack of active N, which may be beneficial for avoiding N-vacancies [19]. Ruffenach et al. [12] investigated the issue and concluded on the basis of high-resolution X-ray diffraction (HRXRD) data that there is no significant difference in crystalline quality between both techniques. They further found that thermal annealing of samples grown by MOVPE can reduce their electron concentration and increase their mobility to values comparable to those for MBE samples.

2.4 HEMTs

The structure and working principle of a HEMT are slightly different from the one of a Metal Oxide Semiconductor Field Effect Transistor (MOSFET), the most widely

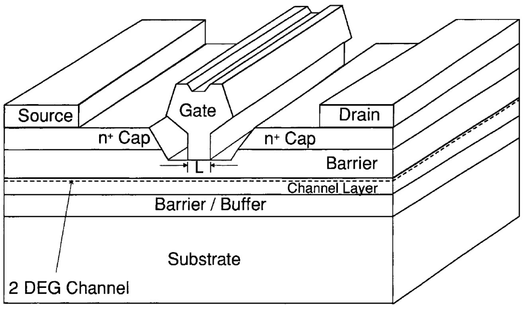

Figure 2.7: Schematic cross-section of a HEMT. The heterojunction at which the 2DEG is located is the interface between the upper barrier and the channel layer. Source, drain and gate form the electric contacts to the device. (from [32])

used transistor in digital electronics. This section explains the device in more detail and discusses materials and figures of merit for HEMTs.

Fig. 2.7 shows the cross-section of a typical HEMT. The most important part of the device is the heterojunction, i.e. a junction formed between two semiconductor materials with different bandgap. This heterojunction is the interface between the upper barrier and the channel layer in fig. 2.7 and fig. 2.8 shows a banddiagram of it before and after the materials are brought into contact. The energies E_c, E_v and E_f are the conduction band minimum, valence band maximum and Fermi level respectively. Because of the different bandgaps, band discontinuities ΔE_c and ΔE_v exist [30].

Upon contacting, the Fermi levels in both materials align. If the two materials have been chosen properly, the band bending at the interface will result in the formation of a triangular well (quantum well) collecting electrons, as illustrated in figure 2.8. This happens because lower energy states are present there. Since the electrons are confined and forced to move in the well in the plane parallel to the interface, they are said to form a two dimensional electron gas (2DEG) [31]. This 2DEG forms a conducting channel between the source and drain of the HEMT. Just as a MOSFET, a HEMT uses the field effect to change the conductivity of the source-drain channel: a third contact, the gate, allows to change the number of electrons in the 2DEG [30].

The electrons occupying the quantum well come from dopants in the large bandgap (barrier) layer (InAlAs in fig. 2.8). It is n-doped, possibly using a thin δ doping layer. On the other hand, the smaller bandgap material (InAlAs in fig. 2.8) is undoped (or unintentionally doped). During the alignment of the Fermi levels, electrons are transferred from the doped layer to the undoped one, forming the 2DEG in the latter. This method to dope a channel with electrons is called modulation doping. It is what makes HEMTs different from MOSFETs and has as advantage that the dopant impurities are physically separated from the carriers. This reduces the Coulomb scattering in the channel, which is beneficial for the mobility [30].

Today, three material systems are used for HEMTs. The first is InAlAs/InGaAs. It can be grown lattice-matched or pseudomorphically on InP or metamorphically on GaAs, in which case the names InP-based and GaAs-based HEMTs are used, respectively. The channel is made of InGaAs. AlGaAs/(In)GaAs forms the second material system. HEMTs in these materials are grown on GaAs substrates (GaAs-

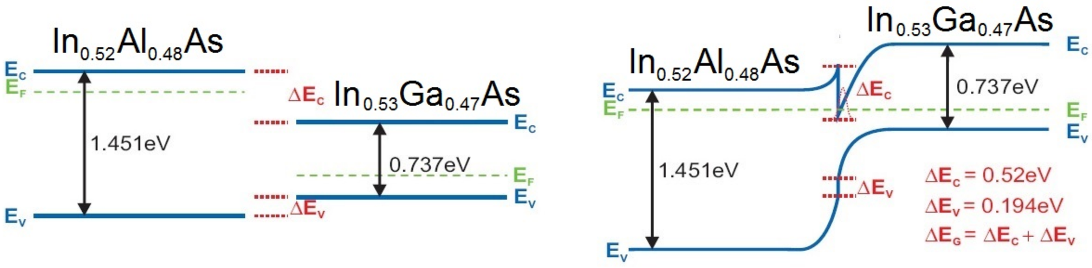

Figure 2.8: Illustration of the formation of a heterojunction between two different semiconductor materials (InAlAs and InGaAs). The left panel shows the materials before contact and the right one after contact. After contact, electrons are confined in the triangular quantum well at the interface in InGaAs. (from [31], slightly adapted)

based HEMTs). The (In)GaAs constitutes the channel. The last material system is AlGaN/GaN or more broadly the III-N semiconductors. Devices in these materials are grown on SiC, sapphire or Si substrates. Recently, also development of GaN substrates for this type of HEMTs was started [16]. A GaN layer forms the channel (GaN HEMTs). InN HEMTs also belong to this category [13].

III-N HEMTs use a mechanism slightly different from the above described modulation doping to dope the 2DEG with electrons [30]. This paragraph explains the principle using GaN as example, but the same holds for InN HEMTs. As pointed out by Ambacher et al. [23], if AlGaN is grown epitaxially on top of GaN to form a heterojunction, the difference in total polarization P of the top and bottom layer will lead to the formation of a sheet charge density σ at the interface, given by the following equation:

$$\sigma \quad = \quad P(\text{top}) - P(\text{bottom}) \tag{2.2}$$

The AlGaN experiences both spontaneous and piezoelectric polarization, whereas the GaN only experiences spontaneous polarization. If the sheet charge density is positive (which is the case for AlGaN/GaN HEMTs), it will be compensated by electrons, forming a two dimensional electron gas at the interface (2DEG). In this way, HEMTs can be made that do not need intentional doping in the larger bandgap (barrier) layer. According to Ibbetson et al. [33], donor-like surface states at the upper AlGaN interface are the source for the electrons in the 2DEG of AlGaN/GaN HEMTs.

Because of the absence of dopants (and hence Coulomb scattering) in the channel, HEMTs are very fast and used for high-frequency applications. Two important high-frequency figures of merit for transistors are f_t and $f_{\max}$. The current gain cut-off frequency f_t is the frequency at which the current gain of the HEMT becomes unity. In other words, it is the frequency at which the HEMT can no longer amplify the input current. The power gain cut-off frequency $f_{\max}$ is the frequency at which the power gain becomes unity. Table 2.2 lists values for both frequencies for GaN, GaAs and InP HEMTs. The gate length is also indicated since a smaller gate length automatically leads to higher f_t and $f_{\max}$ [13, 30].

Table 2.2: Overview of f_t and $f_{\max}$ of different experimental HEMTs. The abbreviations p, m and lm stand for pseudomorphic, metamorphic and lattice matched respectively. (data from [32, 34])

Type	f_t (GHz)	L (nm)	$f_t \times L$ (GHz µm)	$f_{\max}$ (GHz)	L (nm)
InAlN/AlN/GaN HEMT	114	80	9.12	230	80
AlGaAs/GaAs HEMT	113	100	11.3	151	240
pHEMT on GaAs	152	100	15.2	290	100
mHEMT on GaAs	200	120	24	400	100
lmHEMT on InP	350	30	10.5	455	150
pHEMT on InP	340	50	17	600	100

2.5 Transport models

In simulations of semiconductor devices, different transport models can be used. This section briefly discusses the ones used in this master's thesis. The equations as written here are taken from the software manual [35]. In case different 'versions' of the same equation can be chosen in the software, the corresponding parameters were set so that the equations match the ones in [13].

Transport models consist of partial differential equations: the Poisson equation and a number of balance equations. The latter are supplemented by flux equations. Balance and flux equations always have one version for electrons and one for holes [36]. The Poisson equation reads as follows:

$$\vec{\nabla} \cdot (\epsilon \vec{\nabla} \phi) = -q(p - n + N_D - N_A) + \rho_{\mathrm{P}} \tag{2.3}$$

Here, ϵ is the dielectric constant of the material considered, ϕ the electrostatic potential, q the (positive) elementary charge, n (p) the electron (hole) concentration, N_D (N_A) the concentration of donor (acceptor) dopants and $\rho_{\mathrm{P}} = -\vec{\nabla} \cdot \vec{P}$ the polarization induced charge density with $\vec{P}$ the polarization vector. The Poisson equation is always solved, whereas the specific balance equations included depend on the transport model.

The most simple transport model is drift-diffusion. It solves only one balance equation, the current continuity equation:

$$\vec{\nabla} \cdot \vec{J}_n = qR_{\mathrm{net}} + q\frac{\partial n}{\partial t} \tag{2.4}$$

$$-\vec{\nabla} \cdot \vec{J}_p = qR_{\mathrm{net}} + q\frac{\partial p}{\partial t} \tag{2.5}$$

In words, this equation states that the net concentration change of a carrier type in time in a volume element equals the sum of the difference in current density $\vec{J}_n$ ($\vec{J}_p$) through the surface and the net recombination rate R_{net} inside. The model is supplemented with the following flux equations for $\vec{J}_n$ en $\vec{J}_p$:

$$\vec{J}_n = -nq\mu_n \vec{\nabla} \Phi_n \tag{2.6}$$

$$\vec{J}_p = -pq\mu_p \vec{\nabla} \Phi_p \tag{2.7}$$

Here, μ_n (μ_p) and Φ_n (Φ_p) are the electron (hole) mobility and quasi-Fermi potentials, respectively.

In the three equations of the drift-diffusion model (eq. (2.3), (2.4) and (2.5)), ϕ, n, and p are the unknowns [13]. Since n (p) and Φ_n (Φ_p) are related, one can also solve for the latter instead of the former:

$$n = N_c F_{1/2}\left(\frac{E_{F,n} - E_c}{k_B T}\right) \tag{2.8}$$

$$p = N_v F_{1/2}\left(\frac{E_v - E_{F,p}}{k_B T}\right) \tag{2.9}$$

Here, N_c (N_v) is the conduction (valence) band effective density-of-states, $F_{1/2}$ the Fermi integral of order 1/2, $E_{F,n} = -q\Phi_n$ ($E_{F,p} = -q\Phi_p$) the electron (hole) quasi-Fermi energy, E_c (E_v) the conduction (valence) band minimum (maximum), k_B the Boltzmann constant and T the temperature. These expressions hold for the general case of Fermi statistics.

The drift-diffusion model is semi-classical [36]. It can be corrected to include quantum effects by using the density-gradient method. This is not a complete quantum mechanical model, but more a phenomenological model that needs to be calibrated against Poisson-Schrödinger computations. It modifies the electron concentration n (eq. (2.8)) by introducing a potential-like quantity Λ_n in the following way:

$$n = N_C F_{1/2}\left(\frac{E_{F,n} - E_c - \Lambda_n}{k_B T_n}\right) \tag{2.10}$$

$$\Lambda_n = -\frac{\gamma\hbar^2}{6m_n}\frac{\nabla^2\sqrt{n}}{\sqrt{n}} \tag{2.11}$$

Here, T_n and m_n are the electron temperature and effective mass, γ a dimensionless fit factor and $\hbar$ the Dirac constant. A similar expression exists for holes.

In the drift-diffusion model, the electron gas is in thermal equilibrium with the lattice. As a consequence, it cannot describe effects as velocity overshoot and becomes less accurate for devices with gate lengths under 100 nm [36]. The energy transport model can describe these effects. Besides the continuity equation, it solves an additional balance equation, the energy balance equation, and a corresponding additional flux equation, the energy flux equation [13]. Since the model was not used for this master's thesis, it is not discussed here.

In both the drift-diffusion and energy transport model, self-heating of the device can be taken into account by solving the lattice heat flow equation, an additional balance equation. It is supplemented by a flux equation for the lattice energy [13]. Again, the model is not discussed here since it was not used for this thesis.

3

Basic simulation model

The goal of this master's thesis is to build a simulation model for an InN HEMT and estimate the performance of such a device. This simulation model is not built from scratch, but based on existing theoretical proposals for InN HEMTs found in the literature. In particular, the work of Kuzmík and co-workers is used as starting point for this thesis. It is described (in chronological order) in papers [7], [37] and [10].

This chapter describes the implementation of a simulation model for the aforementioned InN HEMT proposal. First, the structure of the InN HEMT is discussed, followed by the basic physical effects included in the model. Then, the results of the basic model are compared with the ones in [10] to verify the correctness of the implementation. Finally, the model is used to calculate the performance of the InN HEMT and some remarks are formulated. The end result is a basic simulation model of an InN HEMT that will be extended in the next chapter.

3.1 Structure of the InN HEMT

In [10], Kuzmík proposes a normally-on and a normally-off N-polar InN HEMT. Both were implemented as basic model for this thesis and this section discusses them more in detail.

The structure of the normally-off HEMT is depicted in fig. 3.1 and is completely taken from [10]. The lowest layer is an N-polar GaN layer, followed by a relaxed $In_{0.9}Al_{0.1}N$ buffer layer. On top of this, a strained GaN spacer is placed. The role of this spacer is to (better) confine the electrons in the channel and to screen possible alloy disorder scattering effects coming from the InAlN buffer. The latter function is similar to the one of the AlN spacer in InAlN/AlN/GaN HEMTs [7, 37]. Next comes the InN channel which is strained with an additional strained GaN spacer on top. This second GaN spacer provides a negative polarization charge at the upper interface of the channel which depletes it from electrons when no gate voltage is applied. Hence, the second spacer is the element that makes the structure a normally-off transistor. A gate oxide, HfO_2 in this case, completes the stack. In [10], Kuzmík proposes both HfO_2 and ZrO_2 as dielectric, but uses ZrO_2 in the calculations. Here, the former material was used since it is more standard and already present in the software. The gate metal is aluminium.

As can be seen in fig. 3.1, the source, drain, gate and bulk contacts are implemented in the simulator as 2D perfect metallic plates (1D lines in the cross-section). In addition to the structure in [10], doped regions with $N_D = 10^{20}$ cm^{-3} were added around the source and drain in order to assure a good contact with the InN channel.

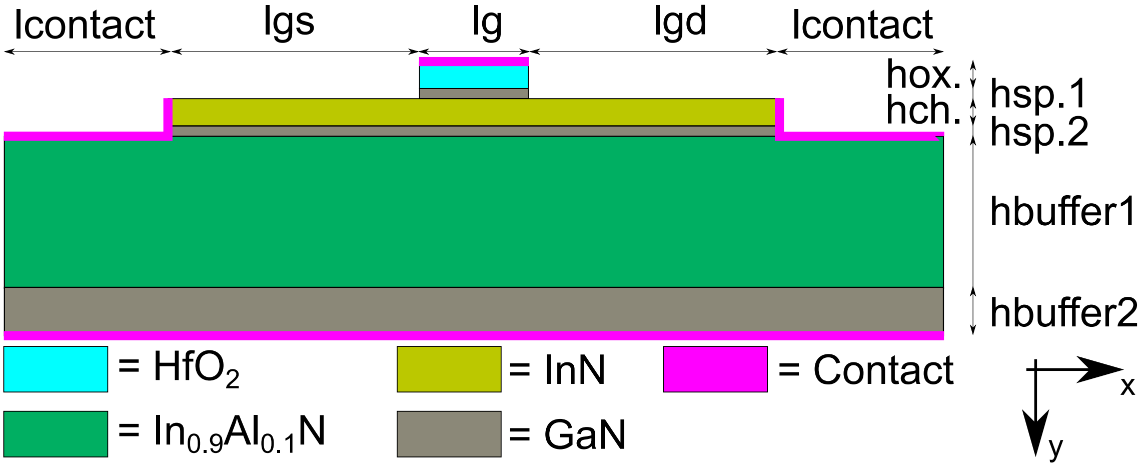

Figure 3.1: Cross-section of the normally-off InN HEMT as implemented in the basic simulation model (not to scale). The normally-on HEMT has the same structure, but without the upper GaN spacer. Table 3.1 lists the different dimensions.

The substrate was not included in the simulations. As mentioned in chapter 2, possible substrates are SiC, sapphire or Si. A mesh of approximately 5000 grid points was defined to solve the transport equations, with the highest density of points located in the channel region.

Table 3.1 indicates the dimensions of the different parts of the InN HEMT, based on [10]. Dimensions not specified in [10] were estimated based on the dimensions of existing HEMT devices, in this case an AlGaAs/InGaAs/AlGaAs HEMT ([13]). The proportionality factor between known dimensions in [10] and the corresponding dimensions in [13] was calculated and then used to calculate the unknown dimensions of the former structure. The two buffer layers (InAlN and lower GaN layer) are relatively thin to reduce the simulation complexity. Since the current flows in the very thin InN channel, this is a reasonable approximation. The source code used to generate the structure of the normally-off HEMT in Sentaurus is included in appendix A.

The structure of the normally-on HEMT is the same as the normally-off one described in fig. 3.1 and table 3.1, but without the GaN spacer between the InN channel and the HfO_2 gate dielectric [10]. Without this layer, the channel is not depleted at zero bias, which implies normally-on operation. The use of the gate dielectric instead of a Schottky gate for both structures has to do with the normally-on HEMT. Experiments on InAlN layers with high In content have indicated that Schottky barrier heights of contacts on these layers are almost zero. Hence, gate insulation is likely to be necessary in InN HEMTs with an InAlN barrier [7] or pure InN on top.

3.2 Basic physical effects included

The basic simulation model for both the normally-on and normally-off transistor includes only a limited number of physical effects. Tables 3.2 and 3.3 list the material parameters used for the binary III-nitrides and HfO_2. The values for ternary alloys

Table 3.1: Horizontal and vertical dimensions (in nm) of the normally-off HEMT as shown in fig. 3.1. For the normally-on HEMT, $h_{\mathrm{sp.1}}$ equals 0.

l_{contact}	250	$h_{\mathrm{ox.}}$	4
l_{gs}	450	$h_{\mathrm{sp.1}}$	0.4
l_{g}	100	$h_{\mathrm{ch.}}$	3
l_{gd}	450	$h_{\mathrm{sp.2}}$	0.6
		h_{buffer1}	200
		h_{buffer2}	60

Table 3.2: Overview of different material parameters used in the basic simulation model. ϵ_r is the relative dielectric constant, χ the electron affinity and ϕ_{barrier} the barrier height of Al on HfO_2 (difference between E_f in Al and E_c in HfO_2). All the other symbols are as previously defined. For parameters related to polarization, + is for N-polar layers and − for cation-polar ones. Values for AlN, GaN and InN come from [10] and for HfO_2 from [38, 39] or are standard values in the software.

	AlN	GaN	InN	HfO_2
ϵ_r (/)	8.5	8.9	15.3	22
$P_{\mathrm{SP},y}$ (10^{-6} C cm^{-2})	± 8.1	± 2.9	± 3.2	-
$(e_{31} - e_{33}(C_{13}/C_{33}))$ (10^{-5} C cm^{-2})	± 8.6	± 6.8	± 9.0	-
a_0 (Å)	3.112	3.189	3.535	-
E_g (eV)	6.2	3.39	0.7	6.0
χ (eV)	-	-	-	2.05
ΔE_c (to GaN) (eV)	-1.7	-	2.1	-1.09
ΔE_c (to InN) (eV)	-3.8	-2.1	-	-2.9
ϕ_{barrier} (eV)	-	-	-	2.3

Table 3.3: Overview of the InN transport parameters used in the basic simulation model. Data for electrons from [10], for holes from [40] (low-field mobility) and [41] (saturation velocity).

$\mu_{\mathrm{low},n}$ (cm^2 V^{-1} s^{-1})	$v_{\mathrm{sat},n}$ (10^7 cm s^{-1})	$\mu_{\mathrm{low},p}$ (cm^2 V^{-1} s^{-1})	$v_{\mathrm{sat},p}$ (10^7 cm s^{-1})
2000	3.5	47.5	0.8

were obtained using Vegard's law [10], i.e. using a linear interpolation of the values for the binary compounds:

$$\text{value}(\text{A}_x\text{B}_{1-x}\text{C}) \;=\; x \times \text{value}(\text{AC}) + (1-x) \times \text{value}(\text{BC}) \tag{3.1}$$

The rest of this section discusses the physical effects described by these parameters. The source code necessary to activate the physical effects (for the normally-off HEMT) in the software is included in appendices B and C.

The first important physical effect is the polarization in the III-N layers. This is incorporated using the strain model based on the work of Ambacher et al. for AlGaN/GaN HEMTs [23, 35]. For the InN HEMT proposed by Kuzmík, the c-axis of the III-N crystals coincides with the y-axis in fig. 3.1. Hence, a polarization vector $\vec{P}$ consisting of a spontaneous and piezoelectric part in the y-direction is introduced. The latter contribution is calculated according to eq. (2.1). The software provides the additional option to modify the strain with a relaxation parameter r varying between 0 and 100%, but here r is assumed 0% for all the layers. Since the InAlN buffer layer is relaxed and the above layers are strained, a in eq. (2.1) equals $a_0(\text{In}_{0.9}\text{Al}_{0.1}\text{N})$ for the channel and spacer layers [37]. The lowest GaN layer is also completely relaxed and hence includes only spontaneous polarization. The polarity of the stack (N-polar) is taken into account by the sign of the spontaneous polarization and the piezoelectric coefficients. N-polarity is not common, cation polarity is much more standard.

Secondly, for the normally-off structure, a processing-dependent negative interface charge was included at the GaN/HfO_2 interface [10] which lowers the positive polarization charge there so that the net charge equals 4×10^{13} e cm^{-2} (e = elementary charge). This processing dependent interface charge is crucial to get enough depletion of electrons in the channel to ensure the normally-off operation. Without it, the HEMT is normally-on. Paper [42] demonstrated for N-polar Al_2O_3/GaN stacks that such compensation of polarization charge is possible. These structures showed a reduction of polarization charge after oxide deposition and a further decrease after post-metallization anneal. The temperature of the anneal could be used to control the amount of compensation. In this thesis, the value of the net positive charge at the interface is chosen differently from that in [10] because of the slightly lower barrier height ϕ_{barrier} of HfO_2 (this work) on Al compared to ZrO_2 ([10]) on Al.

Thirdly, the band discontinuities ΔE_c between the different materials were set to their estimated value. This was done by changing the electron affinity χ of the materials. The electron affinity of HfO_2 was taken as reference and χ of the other materials was calculated using the values for ΔE_c in table 3.2. Remark that this is different for the normally-on and normally-off HEMT. The values for ΔE_c were taken from [10]. Since [10] uses ZrO_2 as gate dielectric and this basic simulation model uses HfO_2, values for ΔE_c between HfO_2 and GaN or InN [38] and ϕ_{barrier} of Al on HfO_2 were searched in the literature. The latter was estimated using the vacuum work function ϕ_{vac} of Al (4.25 eV, [39]) and the pinning factor S (0.52, [38]), charge neutrality level ϕ_{CNL} (4.44 eV, [38]) and electron affinity χ (2.05 eV, standard value software) of HfO_2, according to the formula [38]:

$$\phi_{\mathrm{barrier}} = S\phi_{\mathrm{Al,vac}} + (1-S)\phi_{\mathrm{CNL,HfO_2}} - \chi_{\mathrm{HfO_2}} \tag{3.2}$$

When compared, these values do not differ so much from the ones for ZrO_2. The change of the band gap due to the strain in the III-N layers was ignored for the basic model.

For the velocity-field characteristic ($v(E)$ curve) of InN, a low-field mobility μ_{low} and velocity saturation were combined. For the latter, the Canali/Hänsch formula was used [35]:

$$\mu(E) = \frac{\mu_{\mathrm{low}}}{\left(1+\left(\frac{\mu_{\mathrm{low}}E}{v_{\mathrm{sat}}}\right)^{2.2}\right)^{1/2.2}} \tag{3.3}$$

In this equation, v_{sat} is the saturation velocity and E the driving field, calculated here by taking the gradient of the quasi Fermi potential. Table 3.3 summarizes the different values for these parameters. As can be seen from fig. 2.4, the value for the electron mobility used here has already been observed for InN, but only for thick films ($\approx 10\ \mu$m). The values for hole transport are less important since the device is unipolar and conduction is exclusively by electrons. This was explicitly checked. Table 3.3 contains only values for InN, since only this material forms the channel. It was explicitly checked that the other layers conduct a negligible current. Hence, their transport parameters are less important.

The (electron) $v(E)$ curve represented by eq. (3.3) ($v(E) = \mu(E)E$) gives a smooth transition from a linearly increasing to a constant electron velocity. It is different from both the $v(E)$ curve used in [10] and the one predicted by Monte Carlo simulations, as fig. 3.2 shows. In [10], a two-piece linear $v(E)$ curve was used and Monte Carlo simulations indicate a $v(E)$ curve with a peak. The $v(E)$ curve defined by eq. (3.3) was preferred here since it is more realistic than a two-piece linear approximation. The Monte Carlo $v(E)$ curve should be the most realistic one of all three, since it is obtained by solving the complete Boltzmann transport equation. However, its more complicated shape can cause convergence problems in the simulations and therefore it was not used in the basic model. The value for v_{sat} in the two-piece linear model of [10] is an assumption and is higher than in the $v(E)$ model with peak. This increase was not questioned here and was also used in the basic model. The next chapter on the extended simulation model will investigate the value for v_{sat} more in detail.

Furthermore, Shockley-Read-Hall (SRH) recombination was added to the model. Addition of recombination was necessary to improve the convergence of the simulations, but should not be so important physically since the device is unipolar and the current is dominated by drift. Only SRH recombination was added since this (and not radiative recombination) turns out to be the dominant recombination mechanism at room temperature. This is due to the high concentration of donor-like defects in as-grown InN that act like recombination centres. A recombination time for both electrons and holes of 1 ns was used [43].

Parasitics were taken partially into account by the addition of a gate resistance R_g and a source and drain contact resistance $R_{s,c}$ and $R_{d,c}$. The value of the latter two

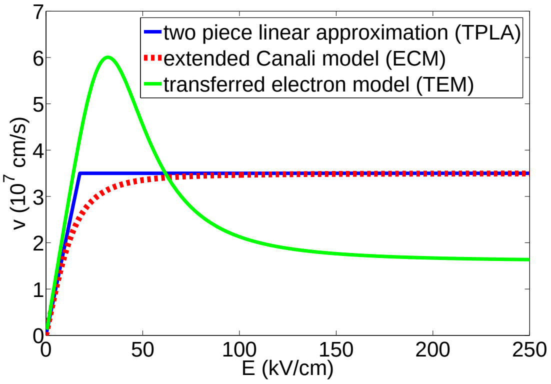

Figure 3.2: Comparison of the different electron $v(E)$ models used in this and other works. The TPLA is used in [10], the ECM here and the TEM is the $v(E)$ curve obtained from steady-state Monte Carlo simulations in [2].

equals 0.1 Ω mm, as in [10]. Other contributions to the total source and drain resistance R_s and R_d are automatically taken into account due to the definition of the device geometry in the simulator. The value of R_g was approximated as the metal part of the gate and calculated based on a gate geometry from [13] rescaled with the gate length. The area of the gate cross-section equals 0.0645 μm^2. Aluminium was taken as the material ($\rho_{\text{Al}} = 2.81 \times 10^{-2}\ \Omega\ \mu\text{m}$ [13]), 50 μm as the gate width and one finger was assumed. In this way, a gate resistance of 7.3 Ω was obtained.

Finally, it has to be noted that Fermi statistics were used and that quantization effects in the direction perpendicular to the channel were not taken into account in the basic simulation model.

3.3 Output and verification of the basic model

DC and AC simulations were carried out for the above described structures. This section summarizes their output and compares where possible to [10], the original InN HEMT proposal. The comparison serves as a verification of the model. Verification with measured data was not possible since there exist (almost) no experimental InN HEMTs.

The DC and AC simulations in the basic model use drift-diffusion. This means that eq. (2.3), (2.4) and (2.5) are solved simultaneously in a coupled way. First, they are solved for zero bias on all four contacts (source, drain, gate and substrate). This allows for the calculation of the band diagram of the structure. Then, for simulation of $I_d(V_d)$ characteristics, the correct gate voltage is applied by solving the same equations after which the drain voltage V_d is ramped from 0 V to a certain maximum value to record the $I_d(V_d)$ curve, as illustrated by the code in appendix B. Something similar is done for simulation of $I_d(V_g)$ curves, but by first applying the correct drain voltage and then ramping the gate voltage.

The calculated band diagrams and electron concentration profiles in the channel under the gate are shown in fig. 3.3 for the normally-off and normally-on structure. They are in very good agreement with the ones in [10]. With respect to the band diagram, the main difference is the oxide (ZrO_2 in [10] and HfO_2 in this work).

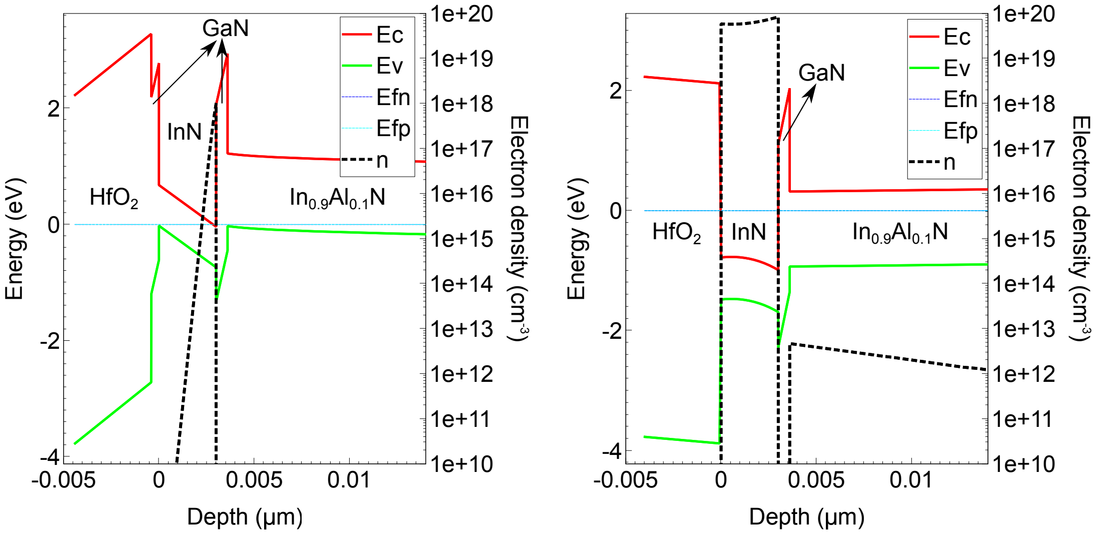

Figure 3.3: Band diagram and electron concentration profile of the normally-off (left) and normally-on (right) HEMT.

Table 3.4: Comparison of the values for the surface polarization charges in the normally-off HEMT in [10] and in this work. The values are in units of 10^{13} e cm^{-2}.

	paper [10]	this work
HfO$_2$/GaN interface	10.1	9.9
GaN/InN interface (upper GaN spacer)	-9.5	-9.2
InN/GaN interface (lower GaN spacer)	9.5	9.2
GaN/In$_{0.9}$Al$_{0.1}$N interface (lower GaN spacer)	-7.8	-7.6
In$_{0.9}$Al$_{0.1}$N/GaN interface (GaN layer on substrate)	-2.3	-0.5
GaN/substrate interface	/	-1.8

The electron concentration profile deviates more. In [10], the peak of the electron concentration is located in the middle of the channel, whereas in this work it lies on the edges of the channel. The explanation is the exclusion of quantization effects in this work. Despite the difference in profile, the sheet charge density n_s in the channel, i.e. the integral of the profile, is very similar in both works. Here, n_s equals 1.9×10^{13} cm^{-2} compared to 2.0×10^{13} cm^{-2} in [10] for the normally-on HEMT. This value is high, but on the order of magnitude for III-N HEMTs [16]. For the normally-off one in this work, n_s is 1.6×10^{10} cm^{-2}. Data for the normally-off are not given in [10].

The values of the surface polarization charges in the normally-off structure in [10] and this work are listed in table 3.4. Again there is very good agreement between both. This should not be so surprising, since both works use the same input parameters and calculation methods for the interface charges. Remark that the charges sum up to 0, as it should.

The $I_d(V_d)$ curves for the normally-off and normally-on HEMT are given in fig. 3.4 and 3.5, respectively. They have the typical form of transistor curves, as it should. The one for the normally-off can be compared with an analytical calculation in [10]. For large V_{gs}, the agreement is good (20% difference), but for smaller V_{gs} the devi-

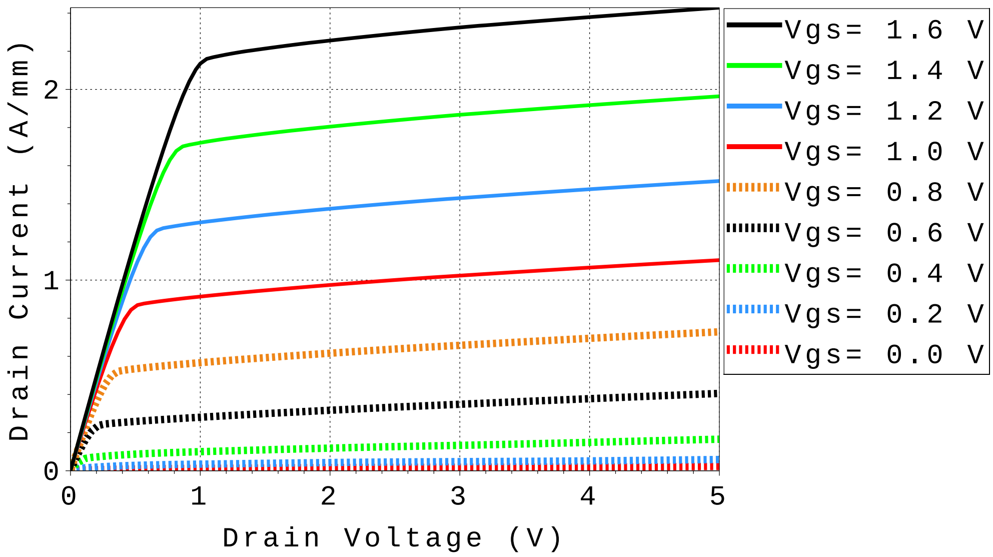

Figure 3.4: $I_d(V_d)$ characteristic of the normally-off HEMT.

ation is larger. Possible explanations for the difference are the fact that the curves in [10] are calculated using an analytical model, whereas the ones in this work are the result of simulations. The latter take automatically more effects into account and start from less assumptions. On the other hand, the analytical model in [10] takes quantization effects partially into account by considering a splitting of the energy levels in the quantum well channel, whereas quantization effects are completed omitted in the basic model here. As already explained, quantization effects have an influence on the carrier concentration profile. The fact that the carriers are located a little bit further away from the interface than classical physics predict reduces the effective gate capacitance and shifts the threshold voltage [35]. Hence, it has an influence close to the off-state, which is the region where the error is largest in this case. Next, velocity saturation is treated differently in both works, as already shown in fig. 3.2. In [10], there is an abrupt change of a mobility of 2000 to 0 $\mathrm{cm^2\ V^{-1}\ s^{-1}}$, whereas in this work, the change is gradual. Finally, the gate oxide is also different (ZrO_2 in [10] and HfO_2 here), but probably this has not such a big influence since both materials are very similar.

The calculated $I_d(V_g)$ curves for both the normally-off and normally-on structure are given in fig. 3.6. They again have the typical form of transistor curves, as it should. From these curves, the threshold voltage V_T and transconductance g_m can be calculated. Table 3.5 lists the values obtained using the $I_d(V_g)$ curve with $V_{ds} = 4$ V. The threshold voltage was determined as the x-intercept of the tangent with the largest slope to the $I_d(V_g)$ curve and for the transconductance the maximum value was taken. There is good agreement between both works. Differences can be attributed to the above described differences in the current-voltage characteristics. In general, the currents and transconductance of the InN HEMT are very large. Paper [34] reports a fabricated (normally-on) GaN HEMT with similar threshold voltage and gate length (80 nm) as the normally-on HEMT here. The maximum transconductance is 0.52 $\mathrm{S\ mm^{-1}}$ and the drain current is 1.1 $\mathrm{A\ mm^{-1}}$ at a higher V_{ds} and V_{gs} than the ones covered in the right panel of fig. 3.6. These values are a

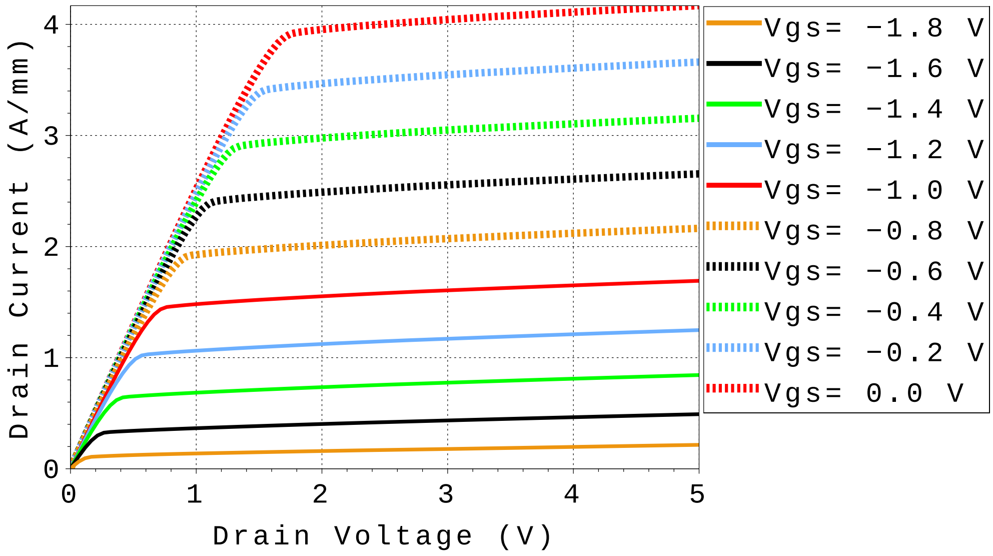

Figure 3.5: $I_d(V_d)$ characteristic of the normally-on HEMT.

Table 3.5: Overview of the threshold voltage V_T and transconductance g_m of the normally-off and normally-on HEMT in [10] and this work. A value for g_m of the normally-on is not given in [10].

	V_T (V)		g_m (S mm^{-1})	
	paper [10]	this work	paper [10]	this work
normally-off	0.5	0.55	3	2.45
normally-on	-1.7	-1.63	-	2.65

lot lower than the ones obtained here. An explanation is the high channel electron density and high saturation velocity of the InN HEMT [10].

From the AC simulations, the S-parameters of the InN HEMT in the basic model could be extracted. They were plotted as an additional way to verify the simulation model by checking if they show (qualitatively) the expected trends. This allows to detect if there is something fundamentally wrong with the model. Fig. 3.7 and 3.8 show the S-parameters for the normally-on HEMT. The frequency range is from 1 MHz to 1 THz (100 MHz to 1 THz in fig. 3.8), the gate width is 50 µm and the bias point is $V_{gs} = -0.19$ V and $V_{ds} = 3$ V, which is in the saturation region.

Most of the S-parameters show the expected behaviour: S_{11} follows more or less a constant resistance circle at low frequencies [44] and S_{21} (related to the voltage gain) is much larger than S_{12} (related to the reverse voltage gain), as it should. The only strange thing is a kink in S_{22} at a frequency of 92.4 GHz. The explanation is the fact that the intrinsic output impedance (i.e. without the output resistance R_{ds}, drain resistance R_d and drain inductance L_d) of a transistor under the measurement conditions of S-parameters (input port matched) intrinsically behaves as a series RC circuit at low frequencies and as a parallel RC circuit at high frequencies, as pointed out in [44]. Hence, S_{22} should follow a 'distorted' constant resistance circle at low frequencies (distorted because of the addition of R_{ds} to the series RC network) and a constant conductance circle at high frequencies. The kink indicates the transition from series to parallel RC circuit behaviour. According to [44], the kink becomes more pronounced if g_m increases, which can explain why it is visible here, since g_m

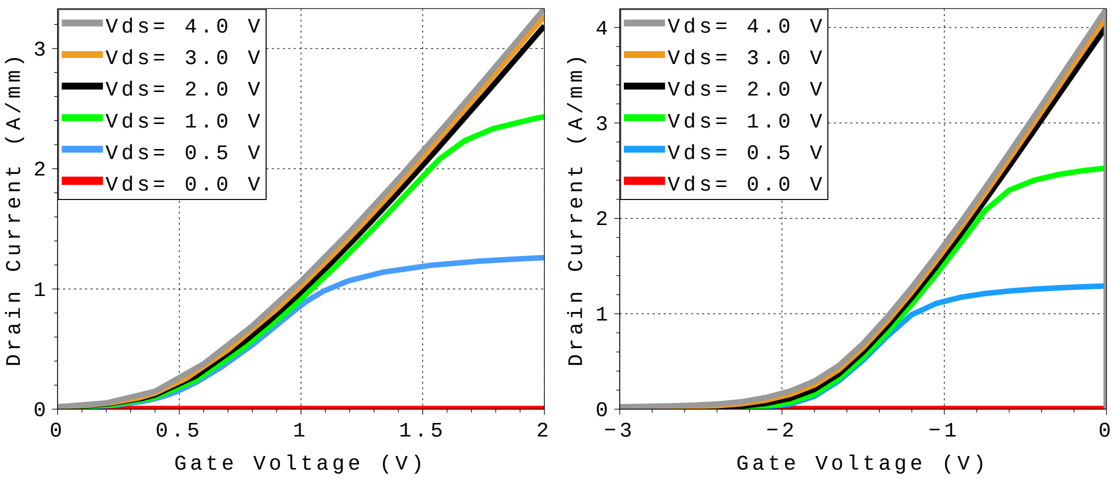

Figure 3.6: $I_d(V_g)$ curves for the normally-off (left) and normally-on (right) HEMT.

is large in this case. The dependence on g_m was explicitly checked by changing the width W of the HEMT and for sufficiently small W (or g_m), the kink disappeared.

3.4 Performance extraction and remarks

From the AC analysis, the current and power gain cut-off frequencies of the InN HEMT were extracted. The first part of this section discusses these figures of merit for the performance of a HEMT.

The current and power gain cut-off frequencies f_t [13] and $f_{\max}$ [45] are defined by the following equations:

$$|h_{21}|_{f=f_t} = 1 \tag{3.4}$$

$$\mathrm{MUG}_{f=f_{\max}} = 1 \tag{3.5}$$

Here, h_{21} is one of the four H-parameters used to describe the small-signal circuit of the HEMT. It is the ratio of the small-signal drain current i_{ds} to the small-signal gate current i_{gs} with the small-signal drain voltage v_{ds} equal to 0, i.e. with the output short-circuited. MUG is Mason's Unilateral Gain and is related to the four Z-parameters [45].

$$h_{21} = \left.\frac{i_{ds}}{i_{gs}}\right|_{v_{ds}=0} \tag{3.6}$$

$$\mathrm{MUG} = \frac{|z_{21}-z_{12}|^2}{4(\Re(z_{11})\Re(z_{22})-\Re(z_{12})\Re(z_{21}))} \tag{3.7}$$

For the power gain cut-off frequency $f_{\max}$, also other definitions exist, but only the one above is used in this thesis.

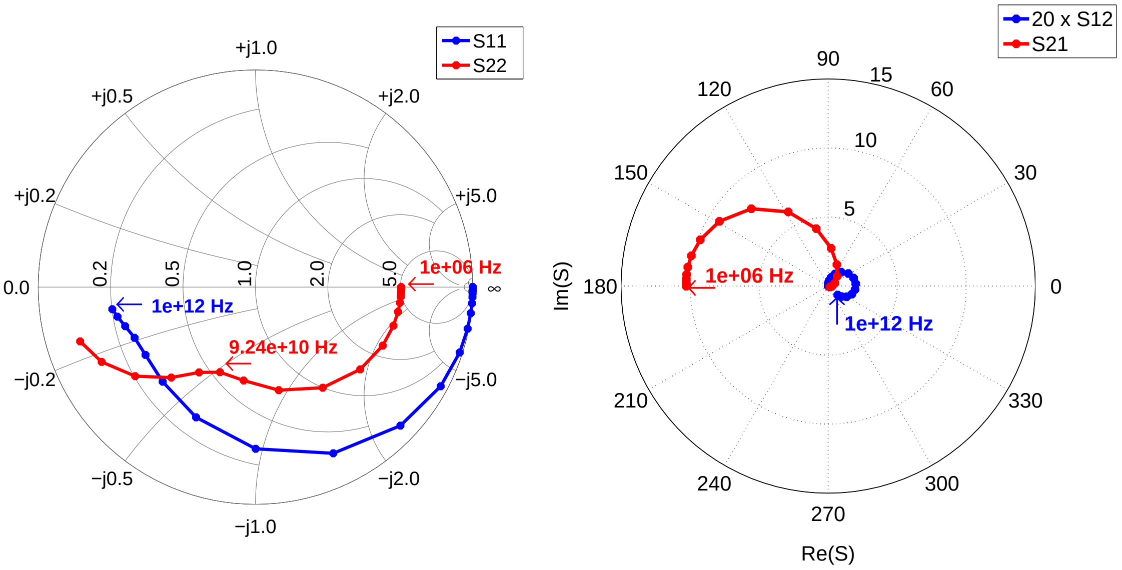

Figure 3.7: Smith chart/polar plot of the S-parameters of the normally-on transistor in the basic model (with the inclusion of a gate resistance and source and drain contact resistance). Start or end frequency of the curves is indicated, total frequency range is from 1 MHz to 1 THz. The bias point is $V_{gs} = -0.19$ V and $V_{ds} = 3$ V, the characteristic impedance Z_0 is 50 Ω and the transistor width W is 50 μm.

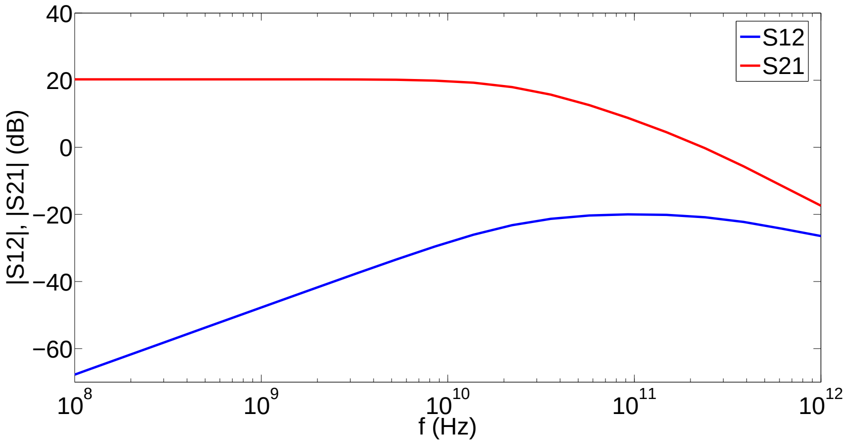

Figure 3.8: Amplitude of the S-parameters S_{12} and S_{21} in dB of the normally-on transistor in the basic model (with the inclusion of a gate resistance and source and drain contact resistance). The bias point is $V_{gs} = -0.19$ V and $V_{ds} = 3$ V, the characteristic impedance Z_0 is 50 Ω and the transistor width W is 50 μm, which is the same as in fig. 3.7

Table 3.6: Overview of f_t and f_{max} of the normally-on transistor in the basic model and the bias point at which the values are obtained, both for the case without and with the inclusion of the gate resistance R_g.

	f_t (GHz)	$f_t \times L$ (GHz µm)	V_{gs} (V)	V_{ds} (V)	$f_{\max}$ (GHz)	V_{gs} (V)	V_{ds} (V)
no R_g	400	40	-0.87	3	720	-0.87	3
R_g	400	40	-0.4	3	430	-0.87	3

Table 3.6 lists the values for f_t and $f_{\max}$ for the normally-on transistor. The analysis was done once without and once with the inclusion of the gate resistance R_g. Both cases include the source and drain contact resistance $R_{s,c}$ and $R_{d,c}$ as before. The extracted frequencies are extremely high. The addition of the gate resistance has a large influence on $f_{\max}$, but not on f_t, as expected.

To understand the reason for the high cut-off frequencies, a simple model for HEMTs from [30] was used. It learns that f_t is determined by the velocity v in the channel and the gate length L as follows:

$$f_t = \frac{v}{2\pi L} \tag{3.8}$$

At a drain-source voltage of 3 V, the magnitude of the electric field at the drain side is approximately 1.6 MV/cm, implying that v equals v_{sat}. By comparing $f_t \times L$ in table 3.6 and 2.2, the influence of L can be taken away. Even then, the values for f_t and $f_{\max}$ are much higher than the ones of experimental HEMTs in other material systems. Hence, the explanation is the high saturation drift velocity (3.5×10^7 cm/s) used in the basic model. As table 1.1 illustrates, the other materials have a lower saturation velocity, the highest being 1.9×10^7 cm/s for GaN. Recall that the value of 3.5×10^7 cm/s for InN was a modified version of the real saturation velocity. Another important point is that table 2.2 lists measured values of real devices. The values for the InN HEMT are the result of simulations. As described in section 3.2, parasitic resistances are taken into account, but pad capacitances not.

Paper [46] reports the analytical calculation of f_t for another InN HEMT. The mobility used there is almost the same as the one here (2100 cm^2 V^{-1} s^{-1}), but the saturation velocity is higher (4.5×10^7 cm/s). For a gate length of 250 nm, an f_t of 160 GHz was found. Rescaling this value with the gate length gives the same result as the f_t obtained in this thesis.

To finalize the discussion about the basic model, the rest of this section lists some remarks about the model and the theoretical proposal it is based on.

Firstly, the basic model in its current form uses ideal parameters which are not realistic when looking to the current state of InN growth, as described in chapter 2. For example, as explained in section 3.2, the low-field mobility of 2000 cm^2 V^{-1} s^{-1} has been observed in grown InN films, but not for the thin (3 nm) films used in this work. Also, the current model does not include the unintentional n-type background doping observed in grown InN films. It uses instead the intrinsic carrier concentration $n_i = p_i = 6.5 \times 10^{12}$ cm^{-3}.

Secondly, some dimensions in the theoretical proposal of [10] are very small, such as the channel thickness of 3 nm and the GaN spacer thickness of 0.4 and 0.6 nm. The dimension of the GaN spacer layers implies fabricating (almost) monolayers of

GaN, since its lattice constant along the *c*-axis is 5.185 Å [16]. Furthermore, the normally-off structure is quite complicated for a basic transistor design. There is the additional GaN spacer and the need of compensation of polarization charge at the oxide-GaN interface in order to have the normally-off working. The simpler structure of the normally-on is, especially for a basic model, an advantage. Finally, the GaN spacers experience very large strain (9.5%), which poses questions about the technical feasibility. A strain of 10% cannot be obtained without appropriate strain engineering and even then it is the extreme limit of what is possible [47].

4

Extended simulation model

This chapter describes the extension of the basic simulation model from the previous chapter. This extension includes addition of extra physical effects, more detailed investigation of the Kuzmík HEMT structure… From here on, only the normally-on HEMT is used.

The first section investigates the origin of the carriers in the Kuzmík HEMT proposal and the addition of quantization effects to the basic model to obtain more realistic carrier concentration profiles. The second section focusses on the mobility model: the low-field mobility and the saturation velocity. This is used to update the performance prediction of the basic simulation model. The last section describes simulations of some other InN HEMT structures, using the simulation deck built in the previous chapter.

4.1 Electrons, holes and quantization effects

4.1.1 Origin of electrons

In the on-state, there is a high electron concentration ($n \approx 8 \times 10^{19}$ cm^{-3}) in the channel. These electrons have to come from somewhere and this section discusses their origin.

According to the theory of Ibbetson et al. [33], in AlGaN/GaN HEMTs the electrons come from donor-like surface states located on the surface of the AlGaN barrier. They fill the GaN quantum well because of the presence of lower energy states and polarization charge there. In the absence of surface states (ideal surface), the AlGaN valence band will act as a donor-like state and supply electrons to the GaN conduction band. This will result in the formation of a two dimensional hole gas (2DHG) at the AlGaN interface.

Initially, no surface states were added to the basic InN HEMT model. In that case, holes accumulating at the bottom of the InAlN buffer layer were observed, as the left panel of fig. 4.1 illustrates. The total number of all positive and negative charges in the structure was integrated to check charge neutrality and it was found that the sum of both components equals zero, as it should. This leads to the conclusion that the holes at the bottom of the InAlN buffer layer act as the source of the electrons, in agreement with the above described theory for GaN HEMTs with ideal surfaces.

In a next step, donor-like states were added at the same place with a density of 10^{14} cm^{-2} and an energy level in the middle of the InAlN band gap. Then,

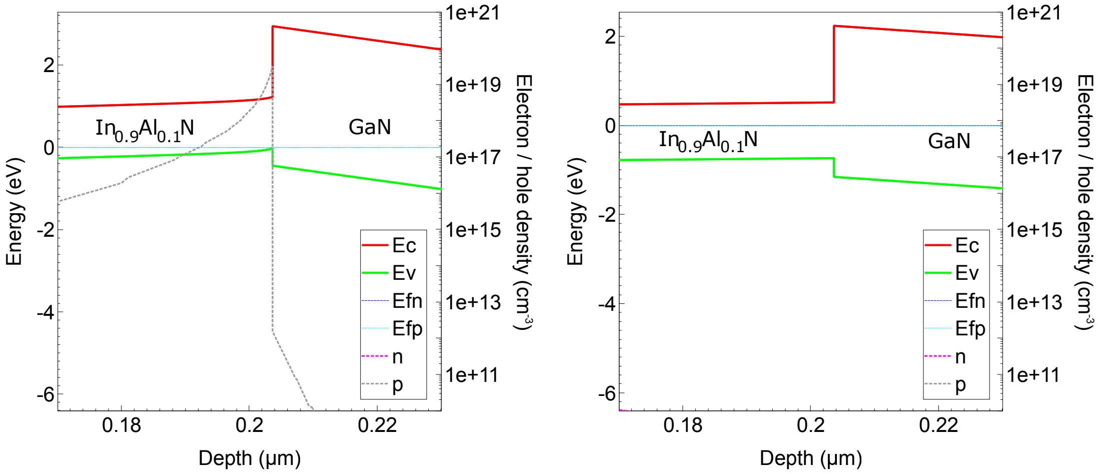

Figure 4.1: Illustration of the 2DHG at the bottom of the InAlN buffer responsible for the electrons in the InN channel. The left panel shows the situation without and the right one with interface states. In the latter case, the 2DHG disappears. Both band diagrams are for zero bias.

the hole gas disappeared, meaning that the donor states now supply the electrons. This is shown in the right panel of fig. 4.1. It was found that the interface states have negligible influence on the electron concentration and current in the on-state (± 2.5%), but a large influence close to the off-state. Due to lack of data on their exact energy level, the interface states were removed again. The energy level is a parameter that will need calibration using data of a real (fabricated) InN HEMT. The influence of the source and drain doping on the electron concentration in the channel was checked as well and found to be non-existing.

As mentioned in chapter 2, all InN layers grown so far suffer from high background electron concentrations. Different mechanisms are considered as explanation for this high n-doping (native defects, unintentional doping by impurities…), but none of them is included in the basic simulation model. It is interesting to note that even then the basic simulation model shows an electron density on the order of the one found in grown InN samples of 3 nm thickness, as can be seen by extrapolating the curve in fig. 2.4. Apparently, in this specific InN HEMT, polarization doping can cause an equally high electron density.

Unintentional doping was added once to the model and in a first step a value of $N_d = 10^{17}$ cm^{-3} was chosen, the lower limit of unintentional doping achievable today (for 1 - 10 μm thick films). Addition of this unintentional doping to the basic model gives no difference with the case without it. The band diagrams, electron concentrations and current levels are the same in both cases, which is logical since an unintentional doping of 10^{17} cm^{-3} is much lower than the polarization doping already present in the channel. Hence, the conclusion is that the InN HEMT described in [10] can function with a level of unintentional doping of 10^{17} cm^{-3} in the channel (e.g. switching the device off is possible).

Increasing the unintentional doping to $N_D = 10^{18}$ cm^{-3} also gives (almost) no difference with the intrinsic case. From doping levels of $N_D = 10^{19}$ cm^{-3} on, the current for a given V_{gs} starts to increase, but there is still gate control. Even larger unintentional doping levels further increase the current.

4.1.2 Quantization effects

As explained in chapter 3, the electron and hole concentration profiles obtained with the basic model are not realistic since they do not go to 0 at the oxide/InN interface or penetrate into the GaN spacer and InAlN buffer. The reason is the use of classical physics everywhere in the device, despite the very small thickness of the channel (3 nm). With respect to the calculated current characteristics, the omission of quantization effects can have an influence on the threshold voltage V_T [35]. Therefore, quantization effects were added in the direction perpendicular to the channel using the density-gradient (DG) method.

As explained in chapter 2, the DG method is only a phenomenological model. More correct would be to solve the Schrödinger equation, but this is computationally very difficult when a bias is applied to the device. In the DG method, eq. (2.10) and (2.11) are solved together with the normal drift-diffusion equations. An important parameter in these equations is the fit factor γ which acts as a correction of the effective mass. Its value can be determined by comparing the carrier concentration profile $n_{\mathrm{DG}}(y)$ obtained using the DG method with $n_{\mathrm{schr.}}(y)$, the one obtained by solving the Poisson and Schrödinger equations self-consistently [48]. For some materials, like GaN, calibration has been carried out in the past and the values are present in the software. For InN, this is not the case since it is a material currently not used in applications. Besides, the calibrated values depend on the thickness of the layers [48], meaning that for the very thin GaN spacer (0.6 nm), the standard value may be incorrect.

As a consequence, a calibration was done for the electron γ parameter of different materials in the InN HEMT: the one of the InN channel and the one of the GaN spacer. The electron concentration profile $n_{\mathrm{schr.}}(y)$ was taken from [10], the original paper of the InN HEMT proposal. The motivation for the omission of the hole calibration is the reduction of the number of fit parameters and the fact that the device is unipolar with the current carried completely by electrons, not by holes. For the holes, the standard γ value for GaN (5.6) was used for both InN and GaN.

The γ factor of these two materials was varied and the resulting electron concentration profile $n_{\mathrm{DG}}(y)$ in the channel under the gate at 0 bias was compared to $n_{\mathrm{schr.}}(y)$. To quantify the accuracy of the fit, the error was calculated as follows:

$$\text{error} = \int |n_{\mathrm{schr.}}(y) - n_{\mathrm{DG}}(y)| \mathrm{d}y \tag{4.1}$$

First, $\gamma_{e^-}(\mathrm{InN})$ was changed in the interval $[0.02, 9]$ while keeping $\gamma_{e^-}(\mathrm{GaN})$ at its standard value of 0.42. In this way, the best value for $\gamma_{e^-}(\mathrm{InN})$ was selected. Then $\gamma_{e^-}(\mathrm{GaN})$ was varied in the same interval while keeping $\gamma_{e^-}(\mathrm{InN})$ at its previously determined value.

Fig. 4.2 shows the results of this procedure. As can be seen in the left panel, it is not possible to find a good fit in the channel. None of the profiles capture the peak around $y \approx 2.5$ nm and most of them result in an electron concentration at the oxide/InN interface that is more than an order of magnitude higher than in [10]. The electron concentration near the oxide can only be reduced at the expense of a global decrease in electron concentration in the channel. For all the γ values, the

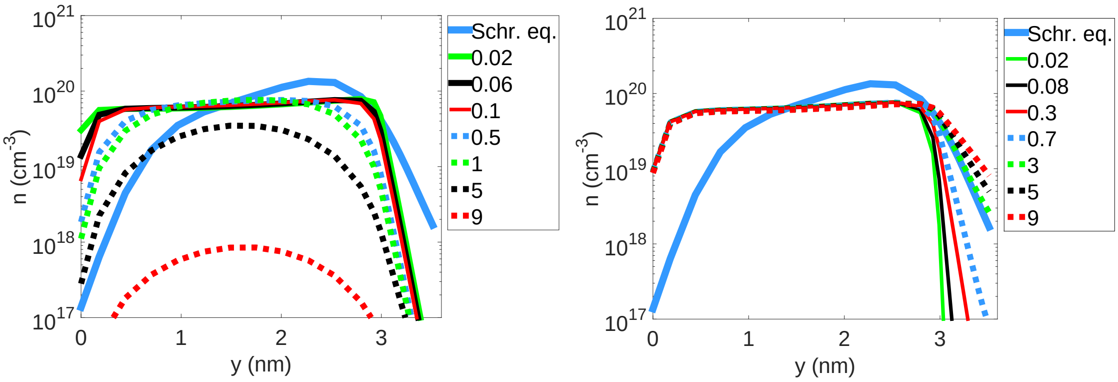

Figure 4.2: Influence of the variation of γ_{e^-}(InN) (left) and γ_{e^-}(GaN) (right) on the electron concentration profile in the channel and GaN spacer. The channel runs from 0 to 3 nm, the GaN spacer from 3 to 3.6 nm. For comparison, the correct concentration profile as obtained with Poisson-Schrödinger computations is also shown. In the left panel, γ_{e^-}(GaN) is kept constant (0.42) and in the right one γ_{e^-}(InN) is kept constant (0.1).

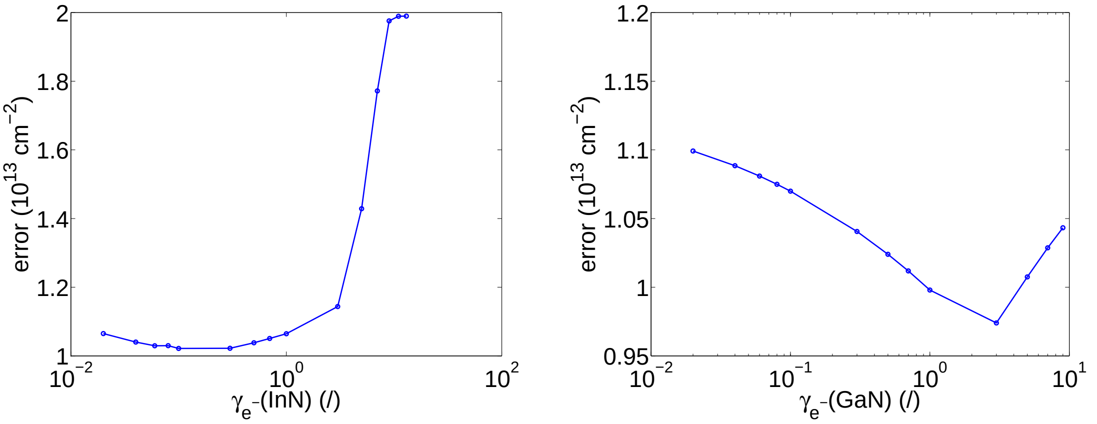

Figure 4.3: Error of the fit of the electron concentration profile versus γ_{e^-}(InN) (left) and γ_{e^-}(GaN) (right).

resulting errors are high, as the left panel of fig. 4.3 illustrates. For large γ_{e^-}(InN) values, the error stagnates at 2×10^{13} cm^{-2} because the difference between $n_{\text{schr.}}$ and n_{DG} has become so large that the error is basically the integral of the former, which equals the sheet charge density. The error varies from 50% to 100% of this sheet charge density. The error is minimal for γ_{e^-}(InN) in the interval $[0.02, 1]$.

For the calibration of γ_{e^-}(GaN), γ_{e^-}(InN) was set to 0.1. The right panel in fig. 4.2 and 4.3 illustrates that it was possible to calibrate γ in the GaN spacer by choosing the value 3. However, the total error remains large due to the misfit in the InN channel. Next, γ_{e^-}(InN) was again varied using the new value for γ_{e^-}(GaN), without improvement in the error. A change of γ_{h^+}(InN) was also investigated, but it was found that this parameter has no influence.

The 'smallest' error occurs for the combination of the values $\gamma_{e^-}(\text{InN}) = 0.1$ and $\gamma_{e^-}(\text{GaN}) = 3$. Fig. 4.4 shows the resulting band diagram and electron concentration profile. Compared to fig. 3.3, the band diagram is the same, as it should be. The

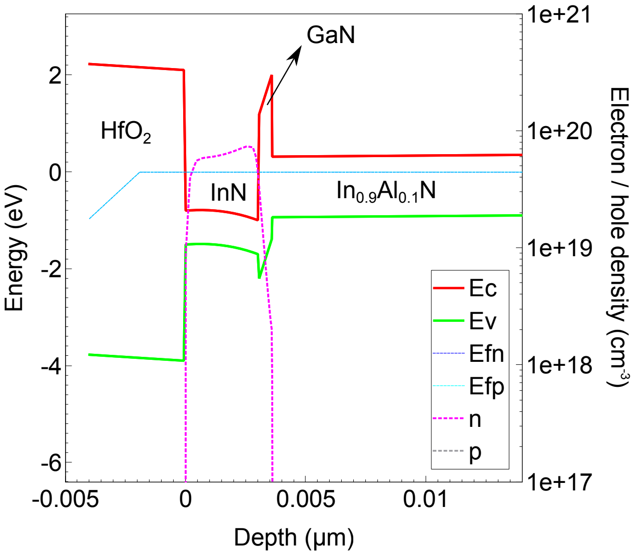

Figure 4.4: Band diagram and electron concentration profile in the channel after the addition of the density gradient method to the model. The profile shows qualitatively the expected features, but there is still a large discrepancy with the correct profile obtained by Schrödinger-Poisson computations.

electron concentration profile in fig. 4.4 is more realistic compared to the ones in chapter 3 since the concentration decreases at the oxide/InN interface and extends partially in the GaN spacer. The sheet charge density n_s in fig. 4.4 equals 1.9×10^{13} cm^{-2}, which is equal to the sheet charge density of the basic model. Compared to the correct concentration profile $n_{\text{schr.}}(y)$, the electrons here are located more in the middle of the InN channel instead of closer to the InN/GaN interface.

A possible solution to obtain the correct concentration profile could be to divide the InN channel in parts (e.g. two parts) and to use a different value for γ in each one. For example, for the first 1 nm of the channel, a value $\gamma^1_{e^-}(\text{InN}) = 5$ would be good (see fig. 4.2), whereas for the other part another value would be more appropriate. This was not done for this thesis since it is already a quite advanced optimization that is probably only useful for this particular structure and that would have to be redone when a new InN HEMT structure is simulated.

4.2 Detailed mobility model

This section considers more at length the mobility model used in chapter 3, since it is an important part of the simulations. As explained earlier, the two main parts of the mobility model are the low-field mobility μ_{low} and the saturation velocity v_{sat}. The first subsection discusses the former and the second the latter. Finally, the last subsection updates f_t and $f_{\max}$ calculated in the previous chapter.

4.2.1 Unintentional doping dependent mobility

As mentioned before, all InN layers grown to date suffer from high unintentional n-doping and the measured low-field mobility varies a lot with the electron concentration in the samples. For the moment, the unintentional doping is unavoidable when growing InN. This section tries to include its effect on the mobility in the simulation model.

Chapter 2 explained that the exact origin of the high background electron concentration in InN is not known. Here, it will be assumed that grown InN is unintentionally doped because of the incorporation of impurities in the material. In that case, the mobility decreases with increasing background electron concentration due to the increasing amount of impurities and ionized impurity scattering. Of the different Monte Carlo studies in table 2.1, only the one of Yarar [5] and Polyakov et al. [3] report results for the mobility as function of the ionized impurity concentration N_d. Both works assume all donors to be ionized and hence the electron concentration n is equal to N_d. The data of Polyakov et al. [3] calculated using the Conwell-Weisskopf approach were selected for this thesis since they correspond best to experimental mobilities for high carrier concentrations ($N_d = n = 10^{17} - 10^{20}$ cm^{-3}). The data of Yarar [5] only go till $N_d = n = 10^{18}$ cm^{-3} and tend to overestimate the experimental data, especially when using the new InN material parameters.

Based on their Monte Carlo simulations and on experimental data, Polyakov et al. propose an empirical model for the mobility in function of the unintentional doping in bulk InN, given by:

$$\mu_{\text{low}} \;=\; \mu_{\text{min}} + \frac{\mu_{\text{max}} - \mu_{\text{min}}}{1 + (N_d/N_{d,\text{ref}})^{\beta}} \tag{4.2}$$

The model was used in this thesis to change the low-field mobility in function of the unintentional doping N_d in the InN channel. A small change was made to the formula proposed by Polyakov et al. The parameter μ_{min} was lowered from 1030 to 100 cm^2 V^{-1} s^{-1} to better describe experimental data. Table 4.1 lists the values of the different parameters in eq. (4.2) and fig. 4.5 shows the model together with the Monte Carlo and experimental data. The latter are a combination of the data in fig. 2.4, without the information about the InN thickness, and data of the first InN samples grown at Chalmers University of Technology [49]. The empirical low-field mobility model coincides very well with the Monte Carlo data and reasonably well with the experimental data. The experimental values are Hall mobilities, which means that the real drift mobility is a factor 1 to 2 lower, depending on the dominant type of scattering [30]. Therefore, it is not a big problem that many of the experimental values lie above the curve of the model/the Monte Carlo data. Remark that for low levels of unintentional doping ($N_d < 10^{17}$ cm^{-3}) the low-field mobility becomes very high, but that these values have not been confirmed yet by experiments.

An important remark is that the experimental data of Chalmers [49] and Lu et al. [12] report the carrier concentration n and not the ionized impurity concentration N_d. SIMS-measurements [50] revealed that the Chalmers samples have a large concentration of impurities in the range of the observed electron concentration, meaning that also there ionized impurity scattering is important and probably $n = N_d$. For the data of Lu et al., the ionized impurity concentration is not known. Hence, by plotting the experimental data of Lu et al. in fig. 4.5, the assumption that $n = N_d$ was made.

Table 4.1: Overview of the values for the different parameters in the empirical model describing the low-field mobility in function of the unintentional doping level for bulk InN (eq. (4.2)). (from [3], slightly adapted)

μ_{min} (cm^2 V^{-1} s^{-1})	100
μ_{max} (cm^2 V^{-1} s^{-1})	14150
$N_{d,\mathrm{ref}}$ (cm^{-3})	2.07×10^{16}
β (/)	0.6959

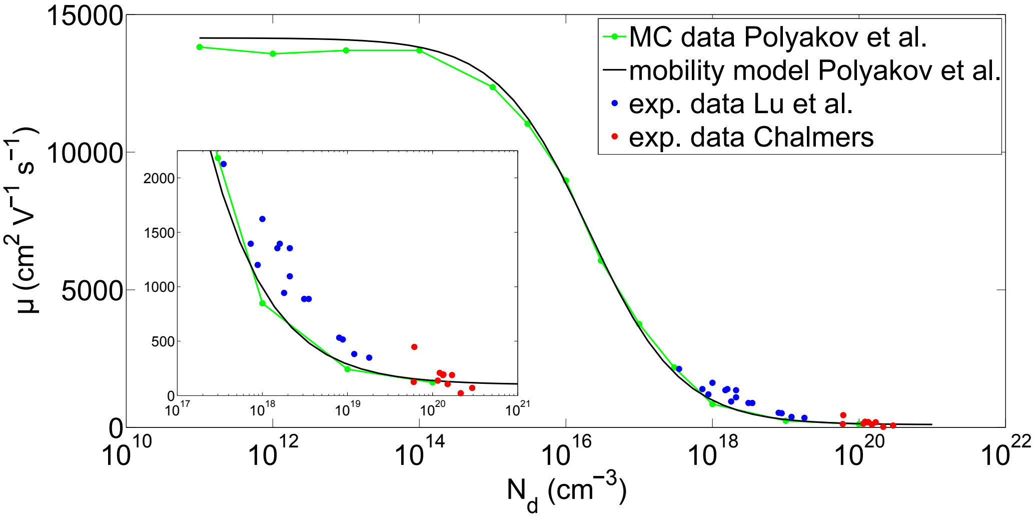

Figure 4.5: Mobility μ versus unintentional doping level/ionized impurity concentration N_d in bulk InN. (data Polyakov et al. from [3], data Lu et al. from [12], data Chalmers from [49])

4.2.2 Saturation velocity

In the basic simulation model, the actual velocity-field characteristic with peak was approximated by a model without peak, as illustrated by fig. 3.2. This section investigates the $v(E)$ curve and value for the saturation velocity v_{sat} more in detail.

The $v(E)$ model with peak, the transferred electron model (TEM), was tried once in the simulations. Using this model, the software had difficulties to accurately simulate in the voltage range when going from linear to saturation region ($V_{ds} = 1-2.4$ V). The $I_d(V_d)$ curves in that region showed sudden dips and peaks. Also, for a few gate voltages, the simulations did not converge. Different things were tried to solve the problem (changing the voltage step ΔV in which the simulator proceeds, 'smoothing' the $v(E)$ curve in the negative differential resistance region…), but it was not possible to make these simulations work properly.

Because of the problems with the TEM, the model without peak was kept. It has the advantage of simplicity. Recall that the saturation velocity in the model without peak was increased with respect to the real v_{sat} and that the new value for v_{sat} is a pure assumption put forward in [10]. A justification for the increase can be trying to compensate the loss of the peak or to take account of the good (predicted) transient electron transport properties (i.e. velocity overshoot) of InN. The latter means that one compensates the fact that the drift-diffusion model cannot describe velocity overshoot (and hence underestimates the current in short gate length devices) by increasing the steady-state saturation velocity.

An attempt was made to investigate this last argument using the energy transport model. As mentioned in chapter 2, this model can take velocity overshoot into account. Contrary to drift-diffusion, in the energy transport model the (high-field) mobility depends on the carrier temperature instead of the electric field, so a $v(E)$ curve is not needed. The necessary parameters to perform simulations are the energy relaxation times $\tau_{\epsilon,n}$ for electrons and $\tau_{\epsilon,p}$ for holes.

However, the (use of the) energy transport model has some limitations. It often overestimates the velocity overshoot [36]. Besides a property of the model itself, the value of the energy relaxation time is often considered part of the problem. Energy relaxation times are bulk material parameters and a down-scaling factor is necessary to convert the bulk to channel value [13]. Determining this factor exactly requires verification of the results of the energy transport model against Monte Carlo simulations of the same device. Such data is not available for the InN HEMT under study. Besides, a lot of parameters in the energy transport equations need to be tuned and their value can also influence the result significantly [35]. Knowledge of these parameter values is again a problem for the InN HEMT under study. Therefore, the use of the energy transport model was not investigated further.

To see the effect of v_{sat} in eq. (3.3) on the simulation results, it was changed once to its real value of 1.6×10^7 cm/s. Fig. 4.6 and 4.7 show the $I_d(V_d)$ and $I_d(V_g)$ curves in that case, respectively. Compared to fig. 3.5 and the right panel of fig. 3.6, the currents are lower, as expected. In the saturation region, the current decreases approximately with a factor 1.6 compared to the situation with v_{sat} equal to 3.5×10^7 cm/s. The conclusion is that the value for v_{sat} in the $v(E)$ curve without peak has an important influence on the simulation results, but that in this master's thesis no answer could be found to the question which value is most appropriate.

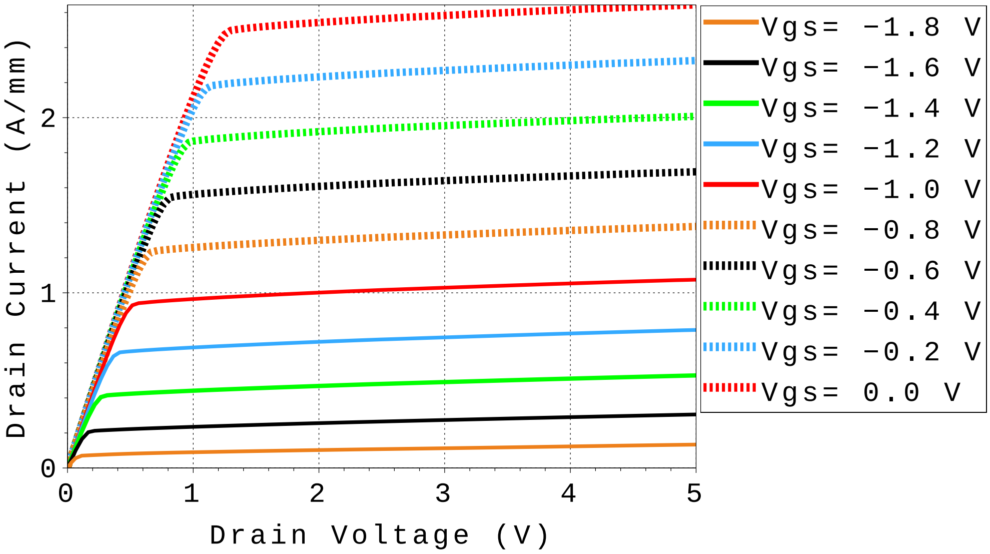

Figure 4.6: $I_d(V_d)$ curve of the normally-on HEMT in the basic model with v_{sat} equal to the real saturation velocity of 1.6×10^7 cm/s.

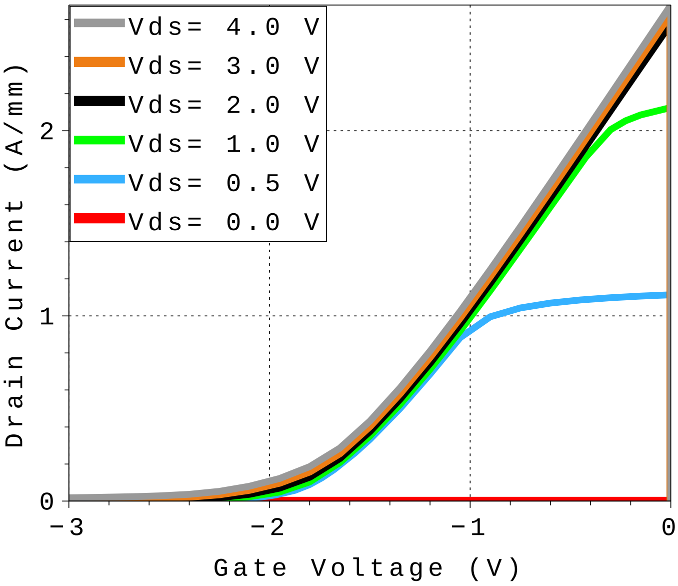

Figure 4.7: $I_d(V_g)$ curve of the normally-on HEMT in the basic model with v_{sat} equal to the real saturation velocity of 1.6×10^7 cm/s.

4.2.3 Updated performance extraction

With the considerations on the mobility model described in this section, the performance prediction of chapter 3 is updated.

For these simulations, the drift-diffusion model with a $v(E)$ curve without peak was used as in the basic model. The two things that were varied were the unintentional doping in the channel (and hence the low-field mobility, see eq. (4.2)) and the saturation velocity. Here, the variation of the saturation velocity is independent of the level of unintentional doping, which is in agreement with reality [13]. The thickness of the InN channel was kept constant at 3 nm, because the InN HEMT structure used here cannot be turned off for thicker channel layers, as will be explained later. Thus, the assumption was made that all unintentional doping levels can be achieved for thin (3 nm) layers. As can be seen in fig. 2.4, this is not the case in reality: ‘low’ levels of unintentional doping are only possible for thick films.

Fig. 4.8 plots f_t and $f_{\max}$ for different levels of the unintentional doping N_d. The corresponding mobilities used in the calculation are indicated as well. Only the concentration range from 10^{17} to 10^{20} cm^{-3} is shown, since these levels have been experimentally observed. Hence, fig. 4.8 gives the possible performance of an InN HEMT based on the current status of InN material growth. The data are given for the real and increased value for v_{sat}. The performance decreases with increasing doping concentration due to the corresponding decrease in mobility.

For $N_d = 3 \times 10^{17}$ cm^{-3}, the mobility is approximately 2000 cm^2 V^{-1} s^{-1}, as in the basic model. Using the real saturation velocity, f_t and $f_{\max}$ become 210 and 260 GHz, respectively. Thus, decreasing v_{sat} by a factor 2 from its increased to its real value divides f_t roughly by a factor 2 as well. This confirms the important role of the value for the saturation velocity on f_t, as pointed out in the previous chapter. For high levels of unintentional doping, the influence of v_{sat} on f_t and $f_{\max}$ decreases. The reason is that the decrease of the low-field mobility increases the electric field at which the electron velocity saturates. As a consequence, a smaller part of the channel has electrons travelling at the saturation velocity and a larger part at a velocity determined by the low-field mobility.

Table 4.2 lists the values for f_t and $f_{\max}$ for an unintentional doping of 10^{14} cm^{-3}. As can be seen in fig. 4.5, this level of unintentional doping has not been observed in InN. According to the Monte Carlo study of Polyakov et al., it should result in the maximum low-field mobility of InN. When comparing with fig. 4.8, these values do not differ so much from the ones for an unintentional doping of 10^{17} cm^{-3}, especially in the case where v_{sat} equals 1.6×10^7 cm^{-3}. The reason is that the high mobility in these cases leads to a larger part of the channel being in velocity saturation. Therefore, the value of the saturation velocity largely determines f_t and $f_{\max}$, more than the low-field mobility (and the level of unintentional doping).

An important remark is that the unintentional doping here only decreases the mobility and does not change the electron concentration in the channel. As discussed in section 4.1.1, the polarization doping in the InN HEMT under study is 10^{20} cm^{-3}. This is higher than or equal to all the levels of unintentional doping observed in InN, meaning that the latter cannot influence the electron concentration. Thus, a mobility observed for bulk InN with a certain background electron concentration is used here in the simulations in a 2DEG with higher actual electron concentration. The

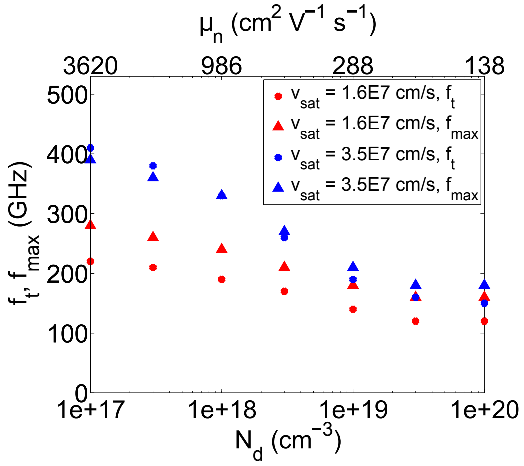

Figure 4.8: Performance of the InN HEMT for different levels of the unintentional doping. The low-field mobility used in the calculations is also added and is given by eq. (4.2). In the simulations, V_{ds} equals 2 V and for V_{gs} the gate-source voltage resulting in maximum f_t or $f_{\max}$ was taken.

Table 4.2: Performance of the InN HEMT for an unintentional doping level of 10^{14} cm^{-3}. This level of unintentional doping has not been achieved in grown InN. In the calculation, V_{ds} equals 2 V and for V_{gs} the gate-source voltage leading to the maximum f_t or $f_{\max}$ was taken.

v_{sat} (10^7 cm/s)	f_t (GHz)	$f_{\max}$ (GHz)
1.6	230	300
3.5	450	410

influence of the additional carriers (e.g. carrier-carrier scattering) on the mobility is neglected. Only the results for $N_d = 10^{20}$ cm^{-3} combine an experimentally observed mobility with the corresponding observed electron concentration in the simulations and hence are the most realistic performance estimate for the HEMT design under study considering the current status of InN growth. In that case, f_t equals 120 (150) GHz and $f_{\max}$ 160 (180) GHz for a saturation velocity of 1.6 (3.5) × 10^7 cm/s.

It is also important to repeat the parasitics taken into account in the calculations. As before, a source and drain contact resistance $R_{s,c}$ and $R_{d,c}$ equal to 0.1 Ω mm are added. Other contributions to the total source and drain resistance R_s and R_d are automatically included in the simulations due to the definition of the device geometry in the simulator. A gate resistance R_g accounting for the metal part of the gate is also added. It is value equals 7.3 Ω (gate width of 50 μm, 1 finger). Pad capacitances are not taken into account.

4.3 Other InN HEMT structures

4.3.1 InN/GaN structure

The simulation deck built for this thesis was used to simulate InN samples grown at Chalmers University of Technology [49]. The simulations comprise band diagram and carrier concentration calculations to check the measured electron concentration in the samples.

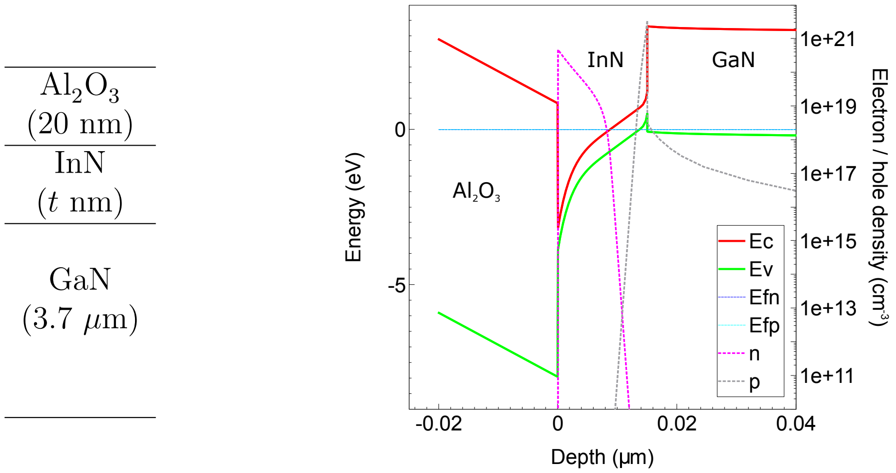

Figure 4.9: Structure (left) and band diagram for $t = 15$ nm (right) of the first InN samples grown at Chalmers University of Technology. The used substrate is sapphire and all the III-N layers have cation polarity. In the right panel, InN is completely strained.

Table 4.3: Material parameters for Al_2O_3. (data from [38, 51, 52])

ϵ_r (/)	E_g (eV)	χ (eV)	ΔE_c (to InN) (eV)	ϕ_{barrier} (eV)
9	8.8	1	-4.0	2.9

As the left panel of fig. 4.9 illustrates, the structure of the above mentioned samples is different from the Kuzmík HEMT proposal. The main reason for this is simplicity. Considering the early stage of InN HEMT growth, this is extra important. The fact that all materials in the Chalmers structure are binary is clearly an advantage, especially the absence of a ternary layer under the InN. This buffer layer should be grown quite thick (> 1 μm) in order to be fully relaxed and growing a thick ternary alloy ($In_{0.9}Al_{0.1}N$ in the Kuzmík HEMT proposal) is more difficult than growing a thick binary material [47]. Another important difference is that the samples are In-polar instead of N-polar. In-polarity is much more standard and easier to grow [47]. The gate oxide is Al_2O_3 instead of HfO_2. Table 4.3 gives the material parameters for this new oxide and is a replacement of the last column of table 3.2. For the metal workfunction of the gate metal on top of Al_2O_3, a value of 3.9 eV was assumed. Different samples were made with varying thickness t of the InN layer. The right panel of fig. 4.9 shows the band diagram and carrier concentration profiles of one of these structures.

Fig. 4.10 compares the calculated and measured sheet charge density n_s of the samples. For the calculation, three scenarios are shown. All of them assume In-polar, intrinsic (i.e. without unintentional doping) InN. The first scenario further assumes InN relaxed on the GaN buffer, whereas the second and third scenario assume completely strained InN. In the first scenario, the electron sheet density is a strong function of the layer thickness and for the thin layers, there is no significant electron accumulation in the InN. Because of this, the black curve in fig. 4.10 only starts at $t \approx 100$ nm. Also, in the first scenario the electrons are located at the lower side of the InN layer, different than shown in the right panel of fig. 4.9.

Despite the large lattice mismatch between InN and GaN (−9.8%), the assump-

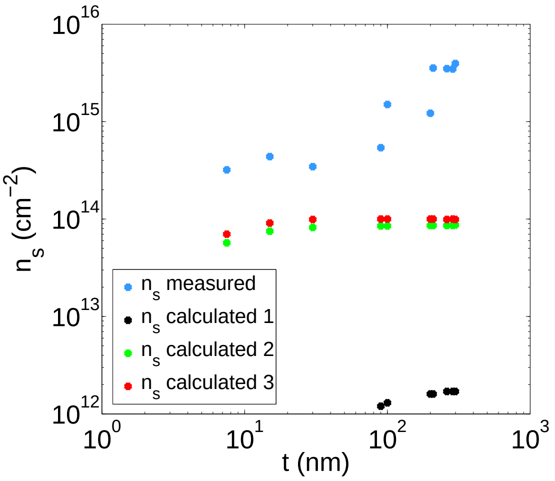

Figure 4.10: Measured and calculated sheet charge density n_s of InN samples versus thickness t of the InN layer. All calculations assume In-polar, intrinsic InN. In the first calculation, InN is completely relaxed. In the second and third one, InN is completely strained and the piezoelectric polarization is calculated using eq. (2.1) and (4.3), respectively.

tion of complete strain in scenario 2 and 3 is valid for the very thin layers ($t \approx 10$ nm). The reason is that the strain is compressive and not tensile. For the thicker ones, relaxation will occur, but a high residual strain is still present [47]. In the second scenario, the piezoelectric polarization is calculated using eq. (2.1) which depends linearly on the strain. As pointed out in [53], the piezoelectric polarization P_{PE} varies non-linearly with strain for high strains, leading to an underestimation when using eq. (2.1). Therefore, the third scenario uses the following equation instead [53]:

$$P_{\mathrm{PE}} = -1.373s + 7.559s^2 \tag{4.3}$$

Here, P_{PE} is in C m^{-2} and s is the strain. The measured values in fig. 4.10 are the result of Hall measurements [49].

A first observation when inspecting fig. 4.10 is that the calculated n_s is almost independent of t. This is logical since the sheet charge density mainly compensates the polarization induced charge and the latter is modelled as being independent of t. The calculated n_s is always around the value of the polarization induced charge at the InN/GaN interface (1.9×10^{12} cm^{-2}) for calculation 1 or at oxide-InN interface (9.0×10^{13} and 1.09×10^{14} cm^{-2}) for calculation 2 and 3, respectively. In reality, for intrinsic InN, n_s will depend on t due to the relaxation dependence of the polarization induced charge on t. If this variation is know, it can be taken into account and the calculated n_s should decrease with t. It should interpolate between the curve of calculation 1 and the curve of calculation 2 - 3.

Secondly, the calculated n_s is extremely high, at least in the strained case. While for GaAs and InP HEMTs n_s is typically around $(1-5) \times 10^{12}$ cm^{-2} [32] and for AlGaN/GaN heterostructures around 10^{13} cm^{-2} [16], the values here are around 10^{14} cm^{-2}. By comparing calculation 1 and 2 - 3, it can be seen that the strain is the reason for this high sheet density. Despite the high numbers, the calculated values are still a lot lower than the measured ones.

Table 4.4: Overview of the magnitude of the polarization vector $\vec{P}$ in the III-N layers and the interface charges σ at the interfaces between these layers for the structures grown at Chalmers University of Technology. The piezoelectric polarization is calculated using eq. (2.1).

		Al_2O_3		InN		GaN	
P_{sp} (10^{13} e cm^{-2})		0		-2		-1.81	
P_{pe} (10^{13} e cm^{-2})		0		+11		0	
P_{tot} (10^{13} e cm^{-2})		0		+9		-1.81	
σ (10^{13} e cm^{-2})	0		+9		-10.81		+1.81

An important question is what the reason is for the difference in calculated and measured sheet charge density. In the calculations, quantization effects are not taken into account and this can have an influence on the results. However, this should only be the case for the very thin layers and the effect should disappear for the ticker ones. Besides, in chapter 3 it was observed that despite differences in concentration profile when taking or not taking quantization effects into account, the integral of the profile did not differ very much in both cases. Furthermore, deviations of the layer thickness can have an influence on the result, just as uncertainties in the metal work function. However, after investigation it turned out that this influence is not decisive. Making the gate oxide 5 nm thicker or thinner hardly has an effect. Furthermore, the calculated n_s in case of a metal work function close to the oxide's E_c is only 40% larger than in the case close to the oxide's E_v.

Based on the large difference (factor 3.5 minimum with the strained case), it is more likely that unintentional doping is the reason for the discrepancy. This would explain the increase of measured n_s with t. In that case, the level of unintentional doping would be as high as 10^{20} cm^{-3}. SIMS-measurements indicated that there is indeed a large number of impurities present in the samples with a density comparable to the measured electron concentration [50].

As can be seen in the right panel of fig. 4.9, the electrons are located near the top surface of the InN layer. This is because a positive interface charge is present there, as table 4.4 shows, but this is not the optimal situation. The concept of a HEMT is to have electrons at an abrupt, defect-free interface between two semiconductors to avoid degradation of the electron mobility. To have the electrons at the heterojunction (instead of the oxide/semiconductor interface), several things can be done.

Firstly, instead of In-polarity, N-polarity can be used. This will switch the sign of all the polarizations and polarization induced interface charges in table 4.4 and hence place the positive interface charge and the electrons at the InN/GaN interface. Fig. 4.11 shows the result. Remark that in the specific case of fig. 4.11 the Fermi level is above the conduction band minimum in part of the GaN buffer, resulting in electrons there. For other III-nitrides such as GaN, anion polar layers are not used extensively and are more difficult to make [47]. Therefore, cation polarity is also preferred for InN and the N-polar option is not investigated further.

A second possibility could be to decrease the piezoelectric polarization in the InN layer. As table 4.4 shows, the absence of InN piezoelectric polarization would result in positive interface charge at the InN/GaN interface ($+1.9\times10^{12}$ e cm^{-2}). However, this also implies making the InN layer thicker and more importantly generation of

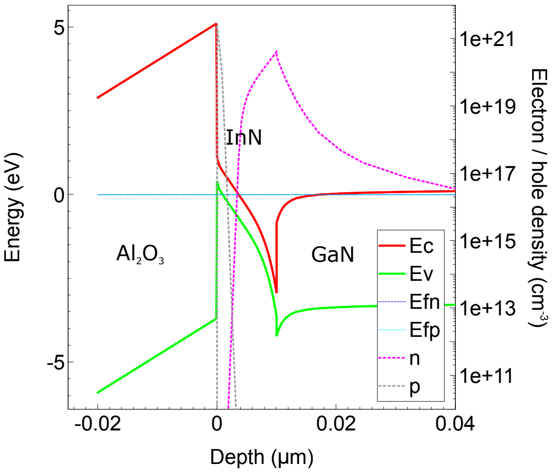

Figure 4.11: Band diagram of the structure as in the left panel of figure 4.9, but with N-polarity for all the III-nitrides. The value for t is 10 nm. Here, InN is completely strained on the GaN buffer.

defects/dislocations at that interface due to the relaxation. This will deteriorate transport properties such as mobility and hence is not considered as an option here. In the simulations, t was increased once and relaxation was introduced in the InN layer. It was observed that the remaining strain should be lower than 5% to have electron accumulation at the InN/GaN interface, implying (almost) complete relaxation.

Next, replacing the GaN buffer for an InGaN or InAlN one could also help to reduce the InN piezoelectric polarization. The reason is that it would decrease the lattice mismatch between InN and the buffer. However, as shown by fig. 2 in [11], there is no value for the In content x in these alloys that makes the interface charge at the InN/buffer interface positive under the assumption of completely strained InN. For relaxed InN, the same argument of dislocations and defects as mentioned above holds.

A last possibility is to simply add a layer on top of the InN. Whereas the previous options tried to place the electrons at an existing heterojunction, this solution provides a heterointerface to the already present electrons. The next subsection will investigate this more in detail.

4.3.2 AlN/InN/GaN structure

Based on the results of the grown samples and on theory, the conclusion was formulated that an additional layer on top of the InN/GaN structure is necessary. This section discusses the specific case of an additional AlN layer. Simplicity again motivates the choice for AlN: it is a binary material and should be easier to grow than a ternary alloy.

The left panel of fig. 4.12 shows the layer sequence of the modified structure with the corresponding vertical dimensions. The gate oxide was removed and replaced with a Schottky gate in order to simplify the structure. Aluminium is the gate metal. The Schottky barrier height of Al on AlN was estimated using eq. (3.2) with

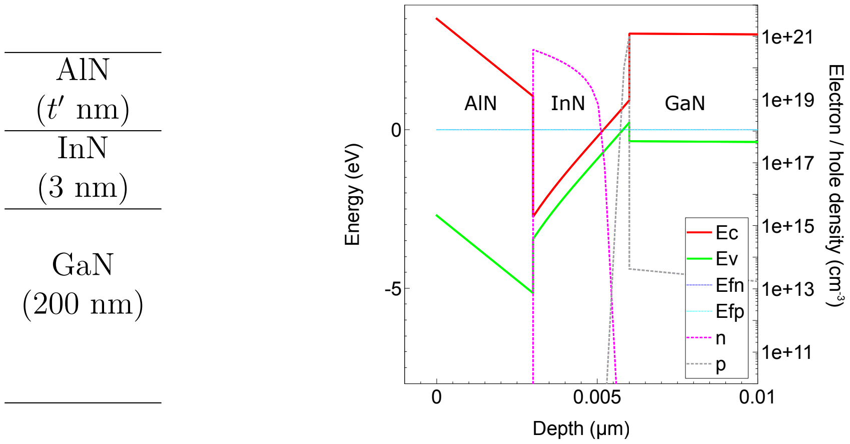

Figure 4.12: Structure (left) and band diagram (right) of the AlN/InN/GaN stack. Horizontal dimensions and contacts are as in the basic simulation model of chapter 3.

the values for HfO_2 replaced by the ones for AlN ($S = 0.41$, $\phi_{\mathrm{CNL}} = 4$ eV and $\chi = 0.6$ eV [38]). All the horizontal dimensions are the same as in the basic simulation model of chapter 3 (table 3.1). The InN layer was assumed to be completely strained on the GaN buffer because of its very small thickness (3 nm). As explained above, experiments done at Chalmers University of Technology [49] showed that this is a correct assumption for very thin InN layers (t ≈ 10 nm) on GaN. The thickness t' of the AlN layer was varied from 1 to 5 nm. Since this is similar to the GaN layer thickness and since the lattice mismatch between GaN and AlN is smaller than the one between GaN an InN, the AlN was also assumed to be completely strained, having a lattice constant equal to the one of GaN.

The right panel of fig. 4.12 shows the band diagram. For all the calculations of the AlN/InN/GaN structure, the linear dependence of piezoelectric polarization on strain is used. The sheet charge density n_s is very high and equals 3.2×10^{13} cm^{-2}. This is lower than n_s calculated for the structures with Al_2O_3 on top (see fig. 4.10), although the latter structure has lower positive polarization charge at the interface with the electrons (see table 4.4 and 4.5). The reason is the thin InN layer in the new structure. Increasing the InN thickness to e.g. 15 nm gives n_s equal to 10.4×10^{13} cm^{-2}, which is higher than $n_s = 7.5 \times 10^{13}$ cm^{-2} for the corresponding structure with Al_2O_3, as expected.

As can be seen in the right panel of fig. 4.12, besides electrons there are also a lot of holes in the channel. They are the source of the electrons and are formed because the Fermi level touches the valence band minimum, as explained in section 4.1.1. Addition of donor-like interface states at the InN/GaN interface again removes these holes since the surface states then supply the electrons.

For the modified structure, $I_d(V_g)$ curves were calculated and they are given in the left panel of fig. 4.13. As can be seen, relative high voltages (higher than in the basic model) are necessary to switch the HEMT off. In the region from −4 to 0 V, there is (almost) no gate control. The threshold voltage V_T equals −7.8 V. The right panel of fig. 4.13 shows the threshold voltage and voltage $V_{g_m=0}$ at which the slope of the $I_d(V_g)$ curve becomes zero versus thickness of the AlN layer. The window

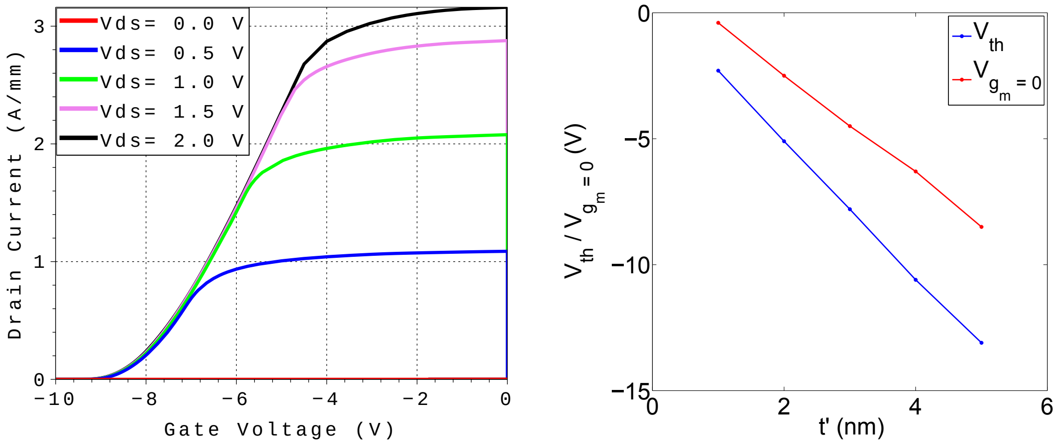

Figure 4.13: $I_d(V_g)$ curves for the AlN/InN/GaN structure (left) and threshold voltage V_T and voltage $V_{g_m=0}$ at which the slope of the $I_d(V_g)$ curve becomes zero versus thickness t' of the AlN layer (right). In the right panel, V_T and $V_{g_m=0}$ are calculated using the $I_d(V_g)$ curve with $V_{\mathrm{ds}} =$ 4 V.

Table 4.5: Overview of the magnitude of the polarization vector $\vec{P}$ in the III-N layers and the interface charges σ at the interfaces between these layers for the AlN/InN/GaN structure.

		AlN		InN		GaN	
P_{sp} (10^{13} e cm^{-2})		-5.1		-2		-1.81	
P_{pe} (10^{13} e cm^{-2})		-2.7		+11		0	
P_{tot} (10^{13} e cm^{-2})		-7.8		+9		-1.81	
σ (10^{13} e cm^{-2})	-7.8		+16.8		-10.81		+1.81

in between both is the region where a HEMT can be biased to work as amplifier. The thinner the AlN layer, the better the gate control and hence the smaller the threshold voltage in absolute value. However, the value of 3 nm is already very thin and can possibly cause gate leakage problems. Given that the transfer characteristic is not good, especially with respect to switch off, and considering that the layers used in the structure are already very thin, the conclusion is that the AlN/InN/GaN stack is not suited for building a HEMT.

The difficulty to switch the HEMT off can be understood by looking at the interface charges in the structure, as given in table 4.5. The positive charge at the InN interface where the electrons are located is very high ($\sigma = 16.8 \times 10^{13}$ e cm^{-2}). When comparing it to the value in table 4.4, it can be seen that it has increased. This is because the strain in the AlN layer is tensile, which makes the piezoelectric polarization in that layer negative and increases the polarization difference with the underlying InN layer having positive polarization. Binary materials were chosen with simplicity as an important motivation. However, it turns out that this leads to high strain. As the right panel of fig. 2.2 illustrates, there is a large lattice mismatch between InN on the one hand and GaN and AlN on the other hand. This leads to very high polarization charges and electron concentrations, making it difficult to switch the HEMT off.

To finalize the discussion on the AlN/InN/GaN structure, it is interesting to note that difficulties in switching the HEMT off were also observed for the structure of

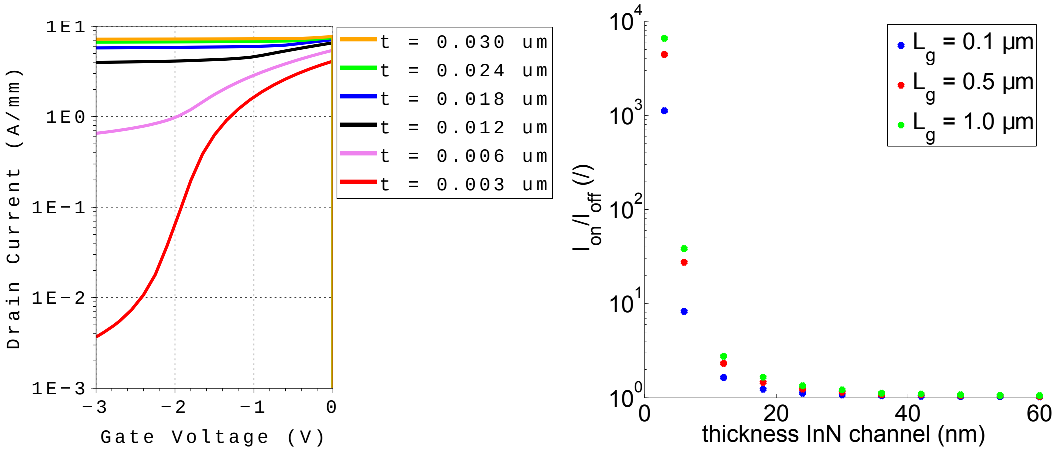

Figure 4.14: $I_d(V_g)$ curve of the Kuzmík InN HEMT proposal for different channel thicknesses t (left). For a channel thickness larger than 3 nm, it becomes difficult to switch the HEMT off. Making the gate longer does not improve the $I_{\text{on}}/I_{\text{off}}$ ratio (right). Here, I_{off} is taken as the current at $V_{gs} = -3$ V.

the basic model in chapter 3. There, the thickness of the InN channel was increased. For a channel thickness only slightly larger than 3 nm, it becomes impossible to turn the HEMT off. This is shown in figure 4.14. Making the gate longer does not improve the switching behaviour. Also here the polarization charge at the location of the electrons (InN/GaN interface) is very high ($\sigma = 9.25 \times 10^{13}$ e cm^{-2}).

5

Conclusions

This master's thesis project dealt with numerical simulations of InN based HEMTs. This last chapter of the thesis summarizes the obtained results. Before doing this, it is good to recapture the actual research question of the thesis: "Which parameters are needed to build a computer model for an InN HEMT, which physical effects should this computer model include and what performance does it predict?" In the introduction, it was explained that this research question comprises two tasks: building a simulation model and using it to estimate the performance of an InN HEMT. Consequently, the conclusion is structured according to these two parts. At the end of the master's thesis project, the simulation model was used briefly to investigate other InN HEMT designs and these results are also summarized here. Finally, the chapter lists some open questions that can be addressed in future research.

5.1 The simulation model

In a first part of this master's thesis project, a basic simulation model for an InN HEMT was built. The structure was taken from the literature [10]. Both a normally-on and normally-off version of the HEMT were implemented. With respect to physical effects, the basic model includes the polarization in the III-N layers, the band discontinuities between the different materials, velocity saturation, (Shockley-Read-Hall) recombination and a parasitic gate resistance and source and drain contact resistance. The basic model does not take quantization effects in the direction perpendicular to the channel into account, although it is only 3 nm thick.

All currents are calculated using the drift-diffusion transport model. For the velocity saturation, a $v(E)$ curve without peak was used as in [10], although Monte Carlo simulations indicate a characteristic with peak. Also, the saturation velocity v_{sat} was increased from the real value of 1.6×10^7 to 3.5×10^7 cm/s. This increase was proposed in [10] and not questioned in the basic model. The shape of the $v(E)$ curve was slightly optimized with respect to the one in [10].

The output of the basic model was analysed and compared to the calculations in the original InN HEMT proposal [10]. This comparison serves as verification of the implementation. Good agreement was found between the band diagrams and electron sheet charge density in both works. The electron concentration profile differs, but this was attributed to the omission of the quantization effects in the basic model. With respect to DC output, the current-voltage characteristics show reasonable agreement with the analytical calculations in [10]. For large V_{gs}, the difference is 20%. This was attributed to the use of analytical formulas versus simulations, the omission of quantization effects in this work, the different mobility model and the different gate oxide.

Using AC simulations, the S-parameters were calculated as an additional way to (qualitatively) verify the basic model. It was found that the S-parameters show the expected behaviour. A kink in S_{22} was observed and could be explained from the different behaviour of the small-signal equivalent circuit at low and high frequencies. The presence of the kink for this specific HEMT was attributed to the high transconductance of the device. Although there is no experimental data to compare the simulation results with, based on the output of the DC and AC calculations, it is reasonable to conclude that the basic simulation model works correctly. It represents one of the first TCAD simulations of an InN HEMT.

In a second part of this master's thesis project, the basic simulation model was extended and subjected to further investigation. It was found that the electrons in the channel come from the valence band at the interface between the InAlN and GaN buffer layer. If donor-like surface states are present at this interface (i.e. the interface is not ideal), than the surface states will be the source of the electrons. Depending on the energy level of the surface states, the holes will disappear.

Quantization effects in the direction perpendicular to the channel were added to the model using the density gradient (DG) method. The objective of this was to obtain more realistic carrier concentration profiles. A good fit of the DG profile to the Poisson-Schrödinger profile could be obtained in the GaN spacer, but not in the (more important) InN channel. The resulting electron concentration profile shows qualitatively the expected trends: it decreases at the oxide/InN interface and extends partially in the GaN spacer. However, the peak is located too far from the InN/GaN interface to coincide with the correct concentration profile.

5.2 Performance and other designs of InN HEMTs

To estimate the InN HEMT performance, the current and power gain cut-off frequencies f_t and $f_{\max}$ were extracted from the AC simulations. For the normally-on HEMT in the basic model of chapter 3, the values are 400 and 430 GHz respectively. Considering the gate length of 100 nm, $f_t \times L$ equals 40 GHz µm. These numbers are extremely high and were attributed to the high (assumed) InN electron saturation velocity of 3.5×10^7 cm/s used in the basic model. The calculation takes a source and drain contact resistance of 0.1 Ω mm and a gate resistance of 7.3 Ω (50 µm gate width, 1 finger) into account. Pad capacitances are not included.

In a next step, the saturation velocity was varied to see the effect on the performance. The parasitics were kept the same. Using the real saturation velocity of InN (1.6×10^7 cm/s) and the same mobility as in the basic model, an f_t of 210 GHz and $f_{\max}$ of 260 GHz were found. This confirms the big influence of the value for the saturation velocity. By running drift-diffusion simulations with a $v(E)$ curve with peak and by energy transport simulations, an attempt was made to investigate which value for the saturation velocity is most appropriate. However, an answer to this question was not found. Hence, the value of 3.5×10^7 cm/s stays an important assumption in the calculations.

Also the mobility was varied and its variation was coupled to the level of unintentional doping observed in bulk InN. For increasing unintentional doping (decreasing low-field mobility), the influence of v_{sat} decreases. An f_t of 120 (150) GHz and $f_{\max}$ of 160 (180) GHz were found for an unintentional doping level of 10^{20} cm^{-3} and a saturation velocity of 1.6×10^7 (3.5×10^7) cm/s. These results combine an experimentally observed mobility with the corresponding observed electron concentration in the simulations and thus are the most realistic performance estimate for the specific HEMT design under study considering the current status of InN growth.

The simulation deck was also used to simulate other InN HEMT structures. Samples consisting of GaN with InN on top as fabricated at Chalmers University of Technology were simulated. It was found that in case of completely strained InN, the calculated electron concentration is very high, but still too low to explain the measured concentration in the samples. It was also concluded that an additional semiconductor material is needed on top of the InN to have the electrons located at a heterojunction. Addition of an extra AlN layer was investigated, but it was found that this AlN/InN/GaN structure is not suited to operate as HEMT due to switch off problems.

5.3 Future outlook

For this master's thesis, a basic InN HEMT simulation model was built and extended. As mentioned in the introduction, research on InN HEMTs is at an early stage. Many things still need to be investigated. One thing is the growth of InN and control of the background electron concentration. With respect to simulations, the following things can be interesting to consider in future work.

First of all, for the simulation model as presented in this thesis, some open questions remain. The electron concentration profile in the channel could not be calibrated with the density gradient method and the value for v_{sat} in the $v(E)$ curve without peak is still based on an assumption. Since the latter has a large influence on f_t and $f_{\max}$, this is important to include in future research. During the investigation of the value for v_{sat} using the energy transport model, the problem of lack of Monte Carlo data was encountered. Therefore, Monte Carlo simulations of an InN HEMT could be useful to decide on a good value for v_{sat} and to learn more about the device in general.

Secondly, there are many additional physical effects not investigated here that could be added to the model. Investigation of breakdown can be interesting considering the InN bandgap of 0.7 eV. This small value suggests a small breakdown voltage for an InN HEMT. Thermal effects can be taken into account in the simulation model as well. In this way, self-heating can be investigated. Finding (reliable) values for different material parameters can be a problem for these simulations.

Besides extensions to the simulation model, it can be useful to investigate additional InN HEMT designs using the simulation deck built in this thesis. At the end of chapter 4, this was started with the simulation of the (AlN/)InN/GaN structure. In that design, the InN is highly strained. To reduce the strain, ternary alloys with high In-content could be tried for the buffer and/or barrier layers. However, these materials are difficult to grow at this moment.

Bibliography

[1] J. A. del Alamo, "The high-electron mobility transistor at 30: impressive accomplishments and exciting prospects," 2011. (`http://www-mtl.mit.edu/~alamo/pdf/2011/RC-189.pdf`, accessed May 14, 2015).

[2] S. K. O'Leary, B. E. Foutz, M. S. Shur, and L. F. Eastman, "Steady-state and transient electron transport within bulk wurtzite indium nitride: an updated semiclassical three-valley Monte Carlo simulation analysis," *Applied Physics Letters*, vol. 87, no. 22, p. 222103, 2005.

[3] V. M. Polyakov and F. Schwierz, "Low-field electron mobility in wurtzite InN," *Applied Physics Letters*, vol. 88, no. 3, p. 032101, 2006.

[4] F. M. Abou El-Ela and B. M. El-Assy, "Electron transport in wurtzite InN," *Pramana*, vol. 79, no. 1, pp. 125–136, 2012.

[5] Z. Yarar, "Transport and mobility properties of wurtzite InN and GaN," *physica status solidi (b)*, vol. 244, no. 10, pp. 3711–3718, 2007.

[6] R. S. Pengelly, S. M. Wood, J. W. Milligan, S. T. Sheppard, and W. L. Pribble, "A review of GaN on SiC high electron-mobility power transistors and MMICs," *IEEE Transactions on Microwave Theory and Techniques*, vol. 60, no. 6, pp. 1764–1783, 2012.

[7] J. Kuzmík and A. Georgakilas, "Proposal of high-electron mobility transistors with strained InN channel," *IEEE Transactions on Electron Devices*, vol. 58, no. 3, pp. 720–724, 2011.

[8] Y. Yue, Z. Hu, J. Guo, B. Sensale-Rodriguez, G. Li, R. Wang, F. Faria, T. Fang, B. Song, X. Gao, *et al.*, "InAlN/AlN/GaN HEMTs with regrown ohmic contacts and f_T of 370 GHz," *IEEE Electron Device Letters*, vol. 33, no. 7, pp. 988–990, 2012.

[9] D. W. Runton, B. Trabert, J. B. Shealy, and R. Vetury, "History of GaN: high-power RF gallium nitride (GaN) from infancy to manufacturable process and beyond," *IEEE Microwave Magazine*, vol. 14, no. 3, pp. 82–93, 2013.

[10] J. Kuzmík, "Proposal of normally-off InN-channel high-electron mobility transistors," *Semiconductor Science and Technology*, vol. 29, no. 3, p. 035015, 2014.

[11] R. Granzner, M. Kittler, F. Schwierz, and V. M. Polyakov, "Vertical design of InN field effect transistors," in *2010 Proceedings of the European Solid-State Device Research Conference (ESSDERC)*, pp. 428–431, IEEE, 2010.

[12] S. Ruffenach, M. Moret, O. Briot, and B. Gil, "Recent advances in the MOVPE growth of indium nitride," *physica status solidi (a)*, vol. 207, no. 1, pp. 9–18, 2010.

[13] V. Palankovski and R. Quay, *Analysis and simulation of heterostructure devices*. Springer, 2004.

[14] Ioffe Institute, "Physical properties of semiconductors." (`http://www.ioffe.rssi.ru/SVA/NSM/Semicond`, accessed March 20, 2015).

[15] M. Heyns, "Compound semiconductors." Lecture notes 'Material Physics and Technology for Nanoelectronics', 2013.

[16] R. Quay, *Gallium nitride electronics*, vol. 96. Springer, 2008.

[17] B. R. Nag, "On the band gap of indium nitride," *physica status solidi (b)*, vol. 237, no. 2, pp. R1–R2, 2003.

[18] V. Y. Davydov, A. A. Klochikhin, V. V. Emtsev, D. A. Kurdyukov, S. V. Ivanov, V. A. Vekshin, F. Bechstedt, J. Furthmüller, J. Aderhold, J. Graul, A. V. Mudryi, H. Harima, A. Hashimoto, A. Yamamoto, and E. E. Haller, "Band gap of hexagonal InN and InGaN alloys," *physica status solidi (b)*, vol. 234, no. 3, pp. 787–795, 2002.

[19] A. G. Bhuiyan, A. Hashimoto, and A. Yamamoto, "Indium nitride (InN): a review on growth, characterization, and properties," *Journal of Applied Physics*, vol. 94, no. 5, pp. 2779–2808, 2003.

[20] K. S. A. Butcher and T. L. Tansley, "InN, latest development and a review of the band-gap controversy," *Superlattices and Microstructures*, vol. 38, no. 1, pp. 1–37, 2005.

[21] J. Wu and W. Walukiewicz, "Band gaps of InN and group III nitride alloys," *Superlattices and Microstructures*, vol. 34, no. 1, pp. 63–75, 2003.

[22] I. Vurgaftman, J. R. Meyer, and L. R. Ram-Mohan, "Band parameters for III–V compound semiconductors and their alloys," *Journal of Applied Physics*, vol. 89, no. 11, pp. 5815–5875, 2001.

[23] O. Ambacher, J. Smart, J. R. Shealy, N. G. Weimann, K. Chu, M. Murphy, W. J. Schaff, L. F. Eastman, R. Dimitrov, L. Wittmer, *et al.*, "Two-dimensional electron gases induced by spontaneous and piezoelectric polarization charges in N- and Ga-face AlGaN/GaN heterostructures," *Journal of Applied Physics*, vol. 85, no. 6, pp. 3222–3233, 1999.

[24] M. Kocan, *AlGaN/GaN MBE 2DEG heterostructures: interplay between surface-, interface-and device-properties.* PhD thesis, Fakultät für Elektrotechnik und Informationstechnik, RWTH Aachen, 2003.

[25] V. W. L. Chin, T. L. Tansley, and T. Osotchan, “Electron mobilities in gallium, indium, and aluminum nitrides,” *Journal of Applied Physics*, vol. 75, no. 11, pp. 7365–7372, 1994.

[26] C. G. Van de Walle, J. L. Lyons, and A. Janotti, “Controlling the conductivity of InN,” *physica status solidi (a)*, vol. 207, no. 5, pp. 1024–1036, 2010.

[27] C. S. Gallinat, G. Koblmüller, and J. S. Speck, “The role of threading dislocations and unintentionally incorporated impurities on the bulk electron conductivity of In-face InN,” *Applied Physics Letters*, vol. 95, no. 2, p. 022103, 2009.

[28] D. W. Jenkins and J. D. Dow, “Electronic structures and doping of InN, $\mathrm{In}_x\mathrm{Ga}_{1-x}\mathrm{N}$, and $\mathrm{In}_x\mathrm{Al}_{1-x}\mathrm{N}$,” *Physical Review B*, vol. 39, no. 5, p. 3317, 1989.

[29] X. Wang, S.-B. Che, Y. Ishitani, and A. Yoshikawa, “Threading dislocations in In-polar InN films and their effects on surface morphology and electrical properties,” *Applied Physics Letters*, vol. 90, no. 15, p. 151901, 2007.

[30] K. F. Brennan and A. S. Brown, *Theory of modern electronic semiconductor devices.* John Wiley, 2002.

[31] Millimeter-Wave Electronics Group, ETH Zürich, “High electron mobility transistors (HEMT),” March 2010. (`http://www.mwe.ee.ethz.ch/en/about-mwe-group/research/vision-and-aim/high-electron-mobility-transistors-hemt.html`, accessed December 28, 2014).

[32] F. Schwierz and J. J. Liou, “Semiconductor devices for RF applications: evolution and current status,” *Microelectronics Reliability*, vol. 41, no. 2, pp. 145–168, 2001.

[33] J. P. Ibbetson, P. T. Fini, K. D. Ness, S. P. DenBaars, J. S. Speck, and U. K. Mishra, “Polarization effects, surface states, and the source of electrons in AlGaN/GaN heterostructure field effect transistors,” *Applied Physics Letters*, vol. 77, no. 2, pp. 250–252, 2000.

[34] B. P. Downey, D. J. Meyer, D. S. Katzer, J. A. Roussos, M. Pan, and X. Gao, “SiN_x/InAlN/AlN/GaN MIS-HEMTs with 10.8 THz V Johnson figure of merit,” *IEEE Electron Device Letters*, vol. 35, no. 5, pp. 527–529, 2014.

[35] Synopsys, *Sentaurus device user guide*, J-2014.09 ed., September 2014.

[36] V. Sverdlov, E. Ungersboeck, H. Kosina, and S. Selberherr, “Current transport models for nanoscale semiconductor devices,” *Materials Science and Engineering: R: Reports*, vol. 58, no. 6, pp. 228–270, 2008.

[37] J. Kuzmík, "N-polarity InN/GaN/InAlN high-electron-mobility transistors," *Applied Physics Express*, vol. 5, no. 4, p. 044101, 2012.

[38] J. Robertson and B. Falabretti, "Band offsets of high K gate oxides on III-V semiconductors," *Journal of Applied Physics*, vol. 100, no. 1, pp. 014111.1–014111.8, 2006.

[39] B. Van Zeghbroeck, "Workfunction in units of eV of selected metals and their measured barrier height on germanium, silicon and gallium arsenide," 2011. (`http://ecee.colorado.edu/~bart/book/book/chapter3/ch3_2.htm`, accessed January 22, 2015).

[40] S. S. Khludkov, I. A. Prudaev, and O. P. Tolbanov, "Physical properties of indium nitride, impurities, and defects," *Russian Physics Journal*, vol. 56, no. 9, pp. 997–1006, 2014.

[41] J. Piprek, *Nitride semiconductor devices: principles and simulation.* John Wiley & Sons, 2007.

[42] T.-H. Hung, S. Krishnamoorthy, M. Esposto, D. N. Nath, P. S. Park, and S. Rajan, "Interface charge engineering at atomic layer deposited dielectric/III-nitride interfaces," *Applied Physics Letters*, vol. 102, no. 7, p. 072105, 2013.

[43] F. Chen, A. N. Cartwright, H. Lu, and W. J. Schaff, "Ultrafast carrier dynamics in InN epilayers," *Journal of Crystal Growth*, vol. 269, no. 1, pp. 10–14, 2004.

[44] S.-S. Lu, C. Meng, T.-W. Chen, and H.-C. Chen, "The origin of the kink phenomenon of transistor scattering parameter S_{22}," *IEEE Transactions on Microwave Theory and Techniques*, vol. 49, no. 2, pp. 333–340, 2001.

[45] Synopsys, *Inspect user guide*, J-2014.09 ed., September 2014.

[46] M. S. Islam, S. M. Muhtadi, M. T. Hasan, A. G. Bhuiyan, M. R. Islam, A. Hashimoto, and A. Yamamoto, "AlInN/InN metal oxide semiconductor heterostructure field effect transistor," *physica status solidi (c)*, vol. 7, no. 7-8, pp. 1983–1987, 2010.

[47] T. Ive, "Private communication on epitaxial growth in general and InN growth in particular." March - April 2015.

[48] P. Andrei, "Calibration of the density-gradient model by using the multidimensional effective-mass Schrödinger equation," *Journal of Computational Electronics*, vol. 5, no. 4, pp. 315–318, 2006.

[49] T. Ive and R. Niklas, "Private communication on the first InN samples fabricated at Chalmers University of Technology." January 2015.

[50] T. Ive, "Private communication on the SIMS-measurements of the first InN samples fabricated at Chalmers University of Technology." April 2015.

[51] M. Heyns, "CO_2 and high-k dielectrics." Lecture notes 'Material Physics and Technology for Nanoelectronics', 2013.

[52] Y.-C. Yeo, T.-J. King, and C. Hu, "Metal-dielectric band alignment and its implications for metal gate complementary metal-oxide-semiconductor technology," *Journal of Applied Physics*, vol. 92, no. 12, pp. 7266–7271, 2002.

[53] O. Ambacher, J. Majewski, C. Miskys, A. Link, M. Hermann, M. Eickhoff, M. Stutzmann, F. Bernardini, V. Fiorentini, V. Tilak, *et al.*, "Pyroelectric properties of Al(In)GaN/GaN hetero- and quantum well structures," *Journal of Physics: Condensed Matter*, vol. 14, no. 13, p. 3399, 2002.

A

Device definition normally-off InN HEMT

This appendix lists the source code used to define the structure of the normally-off InN HEMT in Sentaurus Structure Editor.

```
;----------------------------------------------------------------------;
; TCAD model for InN HEMT as described in paper "Proposal of normally-off
; InN-channel high-electron mobility transistors" by Jan Kuzmik [10]
;----------------------------------------------------------------------;

;------------------------------------------------------;
; INPUTS
; (Values taken from [10] unless stated otherwise)
;------------------------------------------------------;
; vertical dimensions in micrometre
(define hContact 0.025) ; from [13] (fig. A.2, after rescaling)
(define hOxide 0.004)
(define hUpperCap 0.0004)
(define hChannel 0.003)
(define hLowerCap 0.0006)
(define hBuffer 0.2) ; own choice
(define hSeedLayer 0.06) ; own choice

; horizontal dimensions in micrometre
(define lContact 0.25) ; from [13] (fig. A.2, after rescaling)
(define lContactGateSep 0.45) ; [1 (= S/D opening) - 0.1 (= gate length)]/2
(define lGate 0.1)

; In mole fraction in InAlN buffer
(define xAlInN 0.9)

; Source / drain doping
(define dpngSD 1e20)

;--------------------;
; Derived quantities
;--------------------;
; vertical dimensions in micrometre
(define yMin (- 0 hUpperCap hOxide hContact))
(define yOxide (- 0 hUpperCap hOxide))
(define ySD (- 0 hContact))
(define yUC (- 0 hUpperCap))
(define yLC (+ 0 hChannel))
(define yBuffer (+ 0 yLC hLowerCap))
(define ySL (+ 0 yBuffer hBuffer))
(define yMax (+ 0 ySL hSeedLayer))

; horizontal dimensions in micrometre
(define xMin (- 0 lContact lContactGateSep (/ lGate 2)))
(define xSource (- 0 lContactGateSep (/ lGate 2)))
(define xGateL (- 0 (/ lGate 2)))
(define xGateR (- 0 xGateL))
(define xDrain (- 0 xSource))
(define xMax (- 0 xMin))
```

```

;------------------;
; Create structure
;------------------;
(sdegeo:create-rectangle
        (position xGateL yOxide 0) (position xGateR yUC 0)
        "HfO2" "gateDielectric"
)
(sdegeo:create-rectangle
        (position xGateL yUC 0) (position xGateR 0 0)
        "GaN" "upperCapLayer"
)
(sdegeo:create-rectangle
        (position xSource 0 0) (position xDrain yLC 0)
        "InN" "channelLayer"
)
(sdegeo:create-rectangle
        (position xSource yLC 0) (position xDrain yBuffer 0)
        "GaN" "lowerCapLayer"
)
(sdegeo:create-rectangle
        (position xMin yBuffer 0) (position xMax ySL 0)
        "AlInN" "buffer"
)
(sdegeo:create-rectangle
        (position xMin ySL 0) (position xMax yMax 0)
        "GaN" "seedLayer"
)

;--------------------------------------------;
; Set In mole fraction in InAlN buffer
;--------------------------------------------;
(sdedr:define-constant-profile "cpXMoleFractionInAlN" "xMoleFraction" xAlInN)
(sdedr:define-constant-profile-material
        "placeCpXMoleFractionInAlN" "cpXMoleFractionInAlN" "AlInN" 0 "Replace"
)

;-------------------------;
; Place doping profiles
;-------------------------;
(sdedr:define-refinement-window
        "Pl.Source" "Rectangle"
        (position xMin 0 0)
        (position (+ xSource 0.015) 0.025 0)
)
(sdedr:define-constant-profile "P.source" "PhosphorusActiveConcentration" dpngSD)
(sdedr:define-constant-profile-placement "P.source" "P.source" "Pl.Source")

(sdedr:define-refinement-window
        "Pl.Drain" "Rectangle"
        (position (- xDrain 0.015) 0 0)
        (position xMax 0.025 0)
)
(sdedr:define-constant-profile "P.drain" "PhosphorusActiveConcentration" dpngSD)
(sdedr:define-constant-profile-placement "P.drain" "P.drain" "Pl.Drain")

;-------------------------------------;
; Create and place all electrodes
;-------------------------------------;
; source:
(sdegeo:define-contact-set "source")
(sdegeo:set-current-contact-set "source")
(sdegeo:set-contact-edges
        (find-edge-id
                (position (/ (+ xMin xSource) 2) yBuffer 0)
        )
)
(sdegeo:set-contact-edges
        (find-edge-id
                (position xSource (/ yLC 2) 0)
        )
)
(sdegeo:set-contact-edges
        (find-edge-id
                (position xSource (/ (+ yLC yBuffer) 2) 0)
        )
)

; drain:
(sdegeo:define-contact-set "drain")
(sdegeo:set-current-contact-set "drain")
(sdegeo:set-contact-edges
        (find-edge-id
                (position (/ (+ xMax xDrain) 2) yBuffer 0)
        )
)
(sdegeo:set-contact-edges
        (find-edge-id
                (position xDrain (/ yLC 2) 0)
        )
)
(sdegeo:set-contact-edges
        (find-edge-id
                (position xDrain (/ (+ yLC yBuffer) 2) 0)
        )
)

; gate:
(sdegeo:define-contact-set "gate")
(sdegeo:set-current-contact-set "gate")
(sdegeo:set-contact-edges
        (find-edge-id
                (position 0 yOxide 0)
        )
)

; substrate:
(sdegeo:define-contact-set "substrate")
(sdegeo:set-current-contact-set "substrate")
(sdegeo:set-contact-edges
        (find-edge-id
                (position 0 yMax 0)
        )
)

;----------------------------;
; Mesh definition
;----------------------------;
; 1) Default mesh
(sdedr:define-refinement-window
        "defaultMesh" "Rectangle"
        (position xMin yMin 0) (position xMax yMax 0)
)
(sdedr:define-refinement-size "sizeDefaultMesh" 0.1 0.1 99 0.01 0.01 66)
(sdedr:define-refinement-placement
        "placeDefaultMesh" "sizeDefaultMesh" "defaultMesh"
)

; 2) Dense horizontal + vertical grid in channel under gate
(sdedr:define-refinement-window
        "channelMesh" "Rectangle"
        (position (- xGateL 0.050) 0 0) (position (+ xGateR 0.050) (+ yLC 0) 0)
)
(sdedr:define-refinement-size "sizeChannelMesh" 0.01 0.0005 99 0.005 0.0001 66)
(sdedr:define-refinement-placement
        "placeChannelMesh" "sizeChannelMesh" "channelMesh"
)

; 3) Dense horizontal + vertical grid in upper cap layer
(sdedr:define-refinement-window
        "upperCapMesh" "Rectangle"
        (position (- xGateL 0.050) yUC 0) (position (+ xGateR 0.050) 0 0)
)
(sdedr:define-refinement-size "sizeUpperCapMesh" 0.01 0.0001 99 0.005 0.000025 66)
(sdedr:define-refinement-placement
        "placeUpperCapMesh" "sizeUpperCapMesh" "upperCapMesh"
)

; 4) Dense horizontal + vertical grid in lower cap layer under gate
(sdedr:define-refinement-window
        "lowerCapMesh" "Rectangle"
        (position (- xGateL 0.050) yLC 0) (position (+ xGateR 0.050) yBuffer 0)
)
(sdedr:define-refinement-size "sizeLowerCapMesh" 0.01 0.0001 99 0.005 0.000025 66)
(sdedr:define-refinement-placement
        "placeLowerCapMesh" "sizeLowerCapMesh" "lowerCapMesh"
)

; 5) Dense horizontal + vertical grid in channel left of gate
(sdedr:define-refinement-window
        "leftOfGateMesh" "Rectangle"
        (position xMin 0 0) (position (- xGateL 0.040) yLC 0)
)
(sdedr:define-refinement-size "sizeLeftOfGateMesh" 0.01 0.002 99 0.005 0.0005 66)
(sdedr:define-refinement-placement
        "placeLeftOfGateMesh" "sizeLeftOfGateMesh" "leftOfGateMesh"
)

; 6) Dense horizontal + vertical grid in channel right of gate
(sdedr:define-refinement-window
        "rightOfGateMesh" "Rectangle"
        (position (+ xGateR 0.040) 0 0) (position xMax yLC 0)
)
(sdedr:define-refinement-size "sizeRightOfGateMesh" 0.01 0.002 99 0.005 0.0005 66)
(sdedr:define-refinement-placement
        "placeRightOfGateMesh" "sizeRightOfGateMesh" "rightOfGateMesh"
)

; 7) Dense vertical grid at buffer layer - seed layer interface for calculation of
    piezoelectric charge
(sdedr:define-refinement-window
        "blslMesh" "Rectangle"
        (position xMin (- ySL 0.0005) 0) (position xMax (+ ySL 0.0005) 0)
)
(sdedr:define-refinement-size "sizeBlslMesh" 0.1 0.0003 99 0.01 0.0001 66)
(sdedr:define-refinement-placement
        "placeBlslMesh" "sizeBlslMesh" "blslMesh"
)

; 8) Dense vertical grid at bottom of seed layer interface for calculation of
    piezoelectric charge
(sdedr:define-refinement-window
        "bottomSlMesh" "Rectangle"
        (position xMin (- yMax 0.0005) 0) (position xMax yMax 0)
)
(sdedr:define-refinement-size "sizeBottomSlMesh" 0.1 0.0003 99 0.01 0.0001 66)
(sdedr:define-refinement-placement
        "placeBottomSlMesh" "sizeBottomSlMesh" "bottomSlMesh"
)

;----------------------------------------------------------------------;
; Generate and save the structure/mesh using Mesh
;----------------------------------------------------------------------;
(sde:build-mesh "snmesh" "" "n@node@_msh")
```

B

Device simulation normally-off InN HEMT

This appendix lists the source code used to activate the different physical effects in the normally-off InN HEMT and to simulate $I_d(V_d)$ curves of the device.

```
##-------------------------------------------------------------------------------##
## Simulation of InN HEMT as described in paper "Proposal of normally-off
## InN-channel high-electron mobility transistors" by Jan Kuzmik [10]
##-------------------------------------------------------------------------------##

##----------------------------##
## Input and output files
##----------------------------##

File {
        * input files:
        Grid = "@tdr@"
        Parameter = "@parameter@"

        * output files:
        Plot = "@tdrdat@"
        Current = "@plot@"
        Output = "@log@"
}

##----------------------------##
## Definition device
##----------------------------##

Device InNHEMT {

        Electrode {
                {Name="source" Voltage=0.0 AreaFactor = @gateWidth@ Resist = 100}
                {Name="drain" Voltage=0.0 AreaFactor = @gateWidth@ Resist = 100}
                {Name="gate" Voltage=0.0 WorkFunction = 4.37 AreaFactor = @gateWidth@}
                {Name="substrate" Voltage=0.0 AreaFactor = @gateWidth@}
        }
        ## gateWidth in [um], 1000 um used to have output currents in A/mm
        ## Resist in [Ohm um]
        ## Workfunction of aluminium on HfO2

        Physics {
                EffectiveIntrinsicDensity (Nobandgapnarrowing)
                HeteroInterface
                Mobility(ConstantMobility
                        eHighFieldSaturation(CaugheyThomas, GradQuasiFermi)
                        hHighFieldSaturation(CaugheyThomas, GradQuasiFermi)
                )
                Fermi
                Recombination(SRH)
        }

        Physics (MaterialInterface="HfO2/GaN") {
                Traps(FixedCharge Conc=-5.9e13) ## [e/cm^2], -4.9e13 in [10]
        }

        Physics (Region="upperCapLayer") {
                Piezoelectric_Polarization(strain)
        }

        Physics (Material="InN") {
                Piezoelectric_Polarization(strain)
        }

        Physics (Region="lowerCapLayer") {
                Piezoelectric_Polarization(strain)
        }

        Physics (Material="AlInN") {
                Piezoelectric_Polarization(strain)
        }

        Physics (Region="seedLayer") {
                Piezoelectric_Polarization(stress)
        }

        Plot {
                eDensity hDensity
                BandGap
                PE_Charge
                PE_Polarization/Vector
                ConductionBandEnergy ValenceBandEnergy
                eMobility hMobility
                Potential Electricfield/Vector
                eCurrent/Vector hCurrent/Vector TotalCurrent/Vector
                ElectronAffinity
        }
}

##--------##
## Math
##--------##

Math {
        Extrapolate
        CNormPrint
        ExitOnFailure
        ExtendedPrecision       ## No argument (): Long-Double, 128: Double-Double,
                                ## 256: Quad-Double
        Digits=8                ## 15 for 128, 25 for 256
        RHSMin=1e-15            ## 1e-15 for 128, 1e-25 for 256
        Method=Blocked          ## Default method
        SubMethod=Super         ## Default method
}

##--------------------##
## System definition
##--------------------##

System {
        InNHEMT HEMT1 (
                source=0
                gate=nGt
                drain=nDrn
                substrate=0
        )
        Vsource_pset Vgt (nGt 0) {dc = 0}
        Vsource_pset Vdrn (nDrn 0) {dc = 0}
}

##--------##
## Solve
##--------##
```

```

Solve {
        ## Solution for 0 bias:
        Coupled {Poisson}
        Coupled {Poisson Electron Hole Circuit Contact}

        Plot(FilePrefix="n@node@_Zero_Bias")

        Quasistationary (Minstep=1e-5 Goal {Parameter=Vgt."dc" Value=@Vgs@}) {
                Coupled (Iterations=30) {Poisson Electron Hole Circuit Contact}
                Currentplot(Time=(-1))
        }

        Plot(FilePrefix="n@node@_With_Bias_on_Gate")

        Quasistationary (
                Goal {Parameter=Vdrn."dc" Value=@Vds@}
                MinStep=1e-5 MaxStep=0.01 InitialStep=1e-3
        ) {
                Coupled (Iterations=30) {Poisson Electron Hole Circuit Contact}
                Currentplot
                Plot (
                    Fileprefix = "n@node@"
                    Time = (0.0 ; 0.2 ; 0.4 ; 0.6 ; 0.8 ; 1)
                    Nooverwrite
                )
        }
}
```

C

Material parameters normally-off InN HEMT

This appendix lists the source code with the parameters of the different materials used in the normally-off InN HEMT.

```
#define ParFileDir .

##----------------##
## Aluminum
##----------------##

Material="Aluminum" {
        #includeext "ParFileDir/sdevice_Aluminum.par"
}

##----------------##
## HfO2
##----------------##

Material="HfO2" {
        #includeext "ParFileDir/sdevice_HfO2.par"

        Bandgap {
                Eg0 = 6.0       ## [eV] ([52])
                Tpar = 300      ## [K]
                Chi0 = 2.05     ## [eV] (swb)
        }
}

##----------------##
## InN
##----------------##

Material="InN" {
        #includeext "ParFileDir/sdevice_InN.par"

        LatticeParameters {
                X = (1, 0, 0)
                Y = (0, 0, -1)
        }

        Bandgap {
                Eg0 = 0.7       ## [eV] ([10])
                Tpar = 300      ## [K]
                Chi0 = 5.33     ## [eV] (Based on [10] and assumption of workfunction
                                ## of 4.37 eV for aluminium on HfO2) (Chi0 adjusted
                                ## to have DeltaEc as in [10])
        }

        Piezoelectric_Polarization {
                Formula = 2

                psp_z = +3.2e-06        ## [C/cm^2] (+ for N-face) ([23], [10])

                relax = 0.0         ## [1]
                a0 = 3.4927         ## [Angstrom] (In0.9Al0.1N lattice constant) ([10])
                a = 3.535           ## [Angstrom] ([10])

                e31 = 9e-5          ## [C/cm^2] ([10])
                e33 = 0             ## [C/cm^2] ([10])
        }

        ConstantMobility {
                mumax = 2.00e3 , 47.5       ## [cm^2/V/s] ([10] e-, [40] h+)
                Exponent = 0 , 0            ## [1]
        }

        HighFieldDependence {
                Vsat_Formula = 1, 1
                vsat0 = 3.5e7 , 0.8e7       ## [cm/s] ([10] e-, [41] h+)
                vsatexp = 0 , 0             ## [1]
        }
}

##--------------------##
## GaN
##--------------------##

Material="GaN" {
        #includeext "ParFileDir/sdevice_GaN.par"

        LatticeParameters {
                X = (1, 0, 0)
                Y = (0, 0, -1)
        }

        Bandgap {
                Eg0 = 3.39          ## [eV] ([10])
                Tpar = 300          ## [K]
                Chi0 = 3.23         ## [eV] (Based on [10] and assumption of workfunction
                                    ## of 4.37 eV for aluminium on HfO2) (Chi0 adjusted
                                    ## to have DeltaEc as in [10])
        }

        Piezoelectric_Polarization {
                Formula = 2

                psp_z = +2.9e-06            # [C/cm^2] (+ for N-face) ([23], [10])

                relax = 0.0         ## [1]
                a0 = 3.4927         ## [Angstrom] (In0.9Al0.1N lattice constant) ([10])
                a = 3.189           ## [Angstrom] ([10])

                e31 = 6.8e-5        ## [C/cm^2] ([10])
                e33 = 0             ## [C/cm^2] ([10])

                ## stress model is used to calculate (spontaneous) polarization charge in GaN seed layer
                d11 = 0
                d12 = 0
                d13 = 0
                d14 = 0
                d15 = 0
                d16 = 0
                d21 = 0
                d22 = 0
                d23 = 0
                d24 = 0
                d25 = 0
                d26 = 0
                d31 = 0
                d32 = 0
                d33 = 0
                d34 = 0
                d35 = 0
                d36 = 0
        }
}

##--------------------------------------------##
## In_xAl_(1-x)N = Al_(1-x)In_xN
##--------------------------------------------##

Material="AlInN" {
        #includeext "ParFileDir/sdevice_AlInN.par"

        LatticeParameters {
                X = (1, 0, 0)
                Y = (0, 0, -1)
        }

        Bandgap {
                Eg0 = 1.25      ## [eV] ([10])
                Tpar = 300      ## [K]
                Chi0 = 4.95     ## [eV] (Based on [10] and assumption of workfunction
                                ## of 4.37 eV for aluminium on Hf02) (Chi0 adjusted
                                ## to have DeltaEc as in R7)
        }

        Piezoelectric_Polarization {
                Formula = 2

                psp_z = +3.69e-06       ## [C/cm^2] (+ for N-face) ([23], [10])

                relax = 0.0     ## [1]
                a0 = 3.4927     ## [Angstrom] (In0.9Al0.1N lattice constant) ([10])
                a = 3.4927      ## [Angstrom] ([10])

                e31 = 8.96e-5   ## [C/cm^2] ([10])
                e33 = 0         ## [C/cm^2] ([10])
        }
}

##----------------##
## AlN
##----------------##

Material="AlN" {
        #includeext "ParFileDir/sdevice_AlN.par"

        eDOSMass {
                Formula = 2
                Nc300 = 6.235383e18 # [cm^-3] ([14])
        }

        hDOSMass {
                Formula = 2
                Nv300 = 4.884383e20 # [cm^-3] ([14])
        }
}
```